

Probing New Physics in light of recent developments in $b \rightarrow c\ell\nu$ transitions

Tahira Yasmeen^{a,1}, Ishtiaq Ahmed^{b,2}, Saba Shafaq^{a,3}, Muhammad Arslan^{c,4} and Muhammad Jamil Aslam^{c,5}

^a *Department of Physics, International Islamic University, Islamabad 44000, Pakistan.*

^b *National Center for Physics, Islamabad 44000, Pakistan.*

^c *Department of Physics, Quaid-i-Azam University, Islamabad 45320, Pakistan.*

Abstract

At present, experimental studies of the semileptonic B - meson decays at BaBar, Belle and LHCb, especially for the observables associated with the $b \rightarrow c$ transitions, show the deviation from the Standard Model (SM) predictions, consequently, providing a handy tool to probe the possible new physics (NP). In this context, we have first revisited the impact of recent measurements of $R(D^{(*)})$ and $R(\Lambda_c)$ on the parametric space of the NP scenarios. In addition, we have included the $R(J/\psi)$ and the $R(X_c)$ data in the analysis and found that their influence on the best-fit point and the parametric space is mild. Using the recent HFLAV data, after validating the well established sum rule of $R(\Lambda_c)$, we derived the similar sum rule for $R(J/\psi)$. Furthermore, according to the updated data, we have modified the correlation among the different observables, giving us their interesting interdependence. Finally, to discriminate the various NP scenarios, we have plotted the different angular observables and their ratios for $B \rightarrow D^* \tau \nu_\tau$ against the transfer momentum square (q^2), using the 1σ and 2σ parametric space of considered NP scenarios. To see the clear influence of NP on the amplitude of the angular observables, we have also calculated their numerical values in different q^2 bins and shown them through the bar plots. We hope their precise measurements will help to discriminate various NP scenarios.

PACS numbers:

¹ tahira709@gmail.com (corresponding author)

² ishtiaqmusab@gmail.com

³ saba.shafaq@iiu.edu.pk

⁴ arslan.hep@gmail.com

⁵ jamil@qau.edu.pk

I. INTRODUCTION

The SM of particle physics successfully explained most of the experimental measurements; however, in semi-leptonic B -meson decays, 2σ - 4σ level deviations from SM predictions have been observed in recent measurements of $R(D^{(*)})$, $R(J/\psi)$ and the τ polarization asymmetry [1–14]. These observables belong to the $b \rightarrow c\ell\nu_\ell$ transitions occurring through flavor-changing-charged-current (FCCC). Therefore, the observables belonging to the FCCC transitions are an excellent tool to check the SM predictions and to hunt for physics beyond it, i.e., New Physics (NP).

As we know that the theoretical predictions for the decay rates of semileptonic decays bear hadronic uncertainties mainly arising due to the form factors (non-perturbative quantities) and from Cabibbo–Kobayashi–Maskawa (CKM) matrix elements. However, in the ratios such as $R(D^{(*)})$ [15–17], $R(J/\psi)$ [18, 19], $R(X_c)$ [20–22], and $\mathcal{R}(\Lambda_c)$ [23, 24], the dependence on the CKM elements and on the form factor cancels out. From the experimental point of view, the ratios $R(D^{(*)})$, are measured at the BaBar [25, 26], Belle [27–31] and LHCb [32, 33] collaborations and the latest values of HFLAV world average [34] shows an approximately 3.3σ deviations from their SM predictions [25, 26, 35–40]. The other such observables are the ratios of decay rates of B meson decaying to a polarized and unpolarized final state meson, i.e., $P_\tau(D^*)$ and $F_L(D^*)$. Their measurements at the Belle reported $1.5 - 2\sigma$ deviation from their SM results [41–46]. Particularly, $F_L(D^*)$ is important in probing different NP scenarios because the D^* polarizations help us to distinguish between different Lorentz structures (scalar, vector and tensor operators) which influence its value [1]. Similarly, the observable $R(J/\psi)$ has around 2σ deviation from its SM value $\approx 0.23 - 0.29$ [47–54]. Although, its form factors are not precisely known, but to see its current impact on the parametric space, we have included this observable in our analysis. The situation is different for $R(X_c)$, where X_c is an inclusive state involving c quark, which is extensively studied in and beyond the SM [20–22], and its experimental value [40] lies close to the SM predictions.

Additionally, like $R(D^{(*)})$, the LHCb [23] collaboration has recently measured $\mathcal{R}(\Lambda_c)$ in $\Lambda_b \rightarrow \Lambda_c\tau^-\bar{\nu}_\tau$ decays. Its opposite behavior compared to the $R(D^{(*)})$ triggered a lot of theoretical interest, see e.g., [2] for an updated discussion. Finally, because of the lack of accurate measurement of the branching ratio of $B_c^- \rightarrow \tau\nu$ decay, the lifetime of B_c meson put some stringent constraints of the possible NP parameters [44, 55–58]. In this work, for the χ^2 analysis we have used the recent measurements, given in TABLE I, of the seven observables discussed above, i.e., $R(D^{(*)})$, $P_\tau(D^*)$, $F_L(D^*)$, $R(X_c)$, $R(J/\psi)$ and $\mathcal{R}(\Lambda_c)$. For the unobserved decay $B_c^- \rightarrow \tau\nu$, we use the 10%, 30% and 60% upper limits on its branching ratio [59–65] in our analysis.

Perhaps, it is useful to mention that in the earlier attempts the constraint on the parametric space of NP WC's are obtained by considering only the vector or scalar contributions separately [69, 71–74, 77, 78]. However, Blanke *et al.* have done a comprehensive analysis by considering scalar, vector and tensor couplings, but by using only the four experimentally measured observables, namely, $R(D^{(*)})$, $P_\tau(D^*)$ and

$F_L(D^*)$ [1]. Including the recent measurement of $R(\Lambda_c)$ this analysis was revised by Fedele *et al.* [2].

Observables	SM Predictions	Experimental Measurements
$R(D)$	0.298 ± 0.004 [34]	0.357 ± 0.029 HFLAV [34]
$R(D^*)$	0.254 ± 0.005 [34]	0.284 ± 0.012 HFLAV [34]
$P_\tau(D^*)$	-0.497 ± 0.007 [43]	$-0.38 \pm 0.51^{+0.21}_{-0.16}$ [41, 42]
$F_L(D^*)$	0.464 ± 0.003 [66]	$0.60 \pm 0.08 \pm 0.04$ [16]
$R(J/\psi)$	0.258 ± 0.038 [67, 68],	$0.71 \pm 0.17 \pm 0.18$ [18]
$R(X_c)$	0.216 ± 0.003 [69]	0.223 ± 0.030 [69]
$R(\Lambda_c)$	0.324 ± 0.004 [2]	$0.242 \pm 0.026 \pm 0.040 \pm 0.059$ [70]

TABLE I: Different Physical observables, with their experimental measurements and the SM predictions.

The situation is robustly changing; theoretically we have a better control over the uncertainties of the form factors of $B \rightarrow D^{(*)}$ [66, 79] decay, and experimentally after the recent measurements of Belle [80] and LHCb [81, 82] the HFLAV [34] updated their earlier results accordingly. In addition, it will be interesting to redo the analysis by considering these updated values along with the measurements of $R(J/\psi)$, $R(X_c)$ and $R(\Lambda_c)$. For this purpose, we include all the seven observables, mentioned above, together with their updated measurements in our fit analysis which are absent in previous studies [1, 2, 69, 71–74, 77, 78].

With this motivation, the main purpose of this work is not only to explore the allowed parametric space according to the current situation regarding $b \rightarrow c$ transitions but also to see the sensitivity of some angular observables to the NP models which may provide a tool to discriminate among different NP scenarios. To achieve this, we analyse the CP-even angular observables in $B \rightarrow D^* \ell \nu_\ell$ decays and to see their sensitivity on the NP couplings, we plotted them against the invariant dilepton mass q^2 . We have also calculated their numerical values both in different q^2 bins and in the the full q^2 region.

Scheme of our Analysis: Some benchmarks of current analysis are described as:

- To accomplish the goal discussed above, we extend the SM weak effective Hamiltonian (WEH) for the charged current $b \rightarrow c \tau \nu$ by adding the new scalar, vector and tensor type contributions.
- In the current study, the analysis has been done at 2 TeV by using the latest data of all available seven observables $R(D^{(*)})$, $R(J/\psi)$, $F_L(D^*)$, $P_\tau(D^*)$, $R(X_c)$ and $R(\Lambda_c)$. In addition, for the comparison with Blanke *et al.*, plots at 1TeV with updated measurements are also shown. The recipe of the analysis is similar to the Blanke *et al.* [1].
- Based on the choice of observables used for the fitting analysis for NP couplings, we consider the following cases:
 - Fit A: $R(D^{(*)})$, $F_L(D^*)$, $P_\tau(D^*)$

- Fit B: $R(D^{(*)}), F_L(D^*), P_\tau(D^*), R(X_c), R(J/\psi)$,
 - Fit C: $R(D^{(*)}), F_L(D^*), P_\tau(D^*), R(X_c), R(J/\psi), \mathcal{R}(\Lambda_c)$
- We validate the sum rule of $R(\Lambda_c)$ [1, 2], and update it by including the recent theoretical and experimental developments. Similarly, there is a large uncertainty in the value of $R(J/\psi) = 0.71 \pm 0.17 \pm 0.18$ measured by LHCb collaboration [83] and to support the future experimental value with its theoretical predicted value $0.23 - 0.29$, we have also discussed the sum rule of $R(J/\psi)$ in terms of $R(D^{(*)})$.
 - Furthermore, to see the discriminatory power of the observables under consideration, we have also found the correlation among different observables as a function of $R(D^{(*)})$ in different two-dimensional (2D) NP scenarios.
 - Finally, using the 1σ and 2σ intervals of the NP couplings, we will calculate the numerical values of various CP-even observables in $B \rightarrow D^* \tau \nu_\tau$ decay [45, 74–76, 134] and discuss their potential to segregate different NP scenarios. We have also shown bar plots of these angular observables in different bins.

This paper is organized as follows: In Section II, after giving the effective Hamiltonian, we have listed the analytical expressions for the considered observables as a function of NP WCs. The fit procedure which is used to get the allowed values of different NP WCs has also been discussed in the same section. Section III discusses 1D and 2D NP scenarios and their phenomenological analysis of the parametric space. The correlation among the observables and the sum rules are discussed in Section IV. In Section V, we check the sensitivity of CP even angular observables for different NP scenarios and compare their values with the corresponding SM predictions by plotting them against q^2 . Finally, the bar plots are drawn to show their numerical values in different q^2 bins.

II. THEORETICAL FORMULATION

At quark level, we consider the following the WEH for $b \rightarrow c \ell \bar{\nu}_\ell$ transitions

$$\mathcal{H}_{\text{eff}}^{b \rightarrow c \ell \bar{\nu}_\ell} = \frac{4G_F}{\sqrt{2}} V_{cb} \left[(1 + C_V^L) \mathcal{O}_V^L + C_V^R \mathcal{O}_V^R + C_S^R \mathcal{O}_S^R + C_S^L \mathcal{O}_S^L + C_T \mathcal{O}_T \right] + \text{h.c.} \quad (1)$$

where $\ell = \mu, \tau$, G_F is the Fermi constant, V_{cb} is the CKM matrix element and C_i^X are the new WCs with $i = V, S, T$ and $X = L, R$. The corresponding quark level operators \mathcal{O}_i^X are

$$\begin{aligned} \mathcal{O}_S^L &= (\bar{c} P_L b) (\bar{\ell} P_L \nu), & \mathcal{O}_S^R &= (\bar{c} P_R b) (\bar{\ell} P_L \nu), \\ \mathcal{O}_V^L &= (\bar{c} \gamma^\mu P_L b) (\bar{\ell} \gamma_\mu P_L \nu), & \mathcal{O}_V^R &= (\bar{c} \gamma^\mu P_R b) (\bar{\ell} P_L \gamma_\mu \nu), \\ \mathcal{O}_T &= (\bar{c} \sigma^{\mu\nu} P_L b) (\bar{\ell} \sigma_{\mu\nu} P_L \nu), \end{aligned} \quad (2)$$

with $P_L = \frac{1-\gamma_5}{2}$ and $P_R = \frac{1+\gamma_5}{2}$. We know that experimentally no new states beyond the SM have been found so far up to an energy scale of approximately 1TeV, and that measurements of the Higgs couplings are all consistent with the SM expectations, therefore, the right-handed operators do not contribute in the SM [85] making the coupling C_V^R to be universal, which is strongly constrained from $b \rightarrow c(e, \mu)\bar{\nu}_{(e, \mu)}$ data. However, if the assumption of linearity of EWSB is relaxed then one can consider a non-universal C_V^R coupling in the analysis, therefore, we included it and discuss this case separately in our analysis (see detail in ref. [84, 85]). Moreover, in the absence of the experimental evidence of deviations from the SM in the tree-level transitions involving light leptons, it is assumed that the NP effects generally supposed to appear in the third generation of leptons [85].

The new WCs present in Eq. (1) are calculated at 2 TeV, and these are related to $\mu=m_b$ scale as follows [86]:

$$C_V^L(m_b) = 1.12C_V^L(2\text{TeV}), \quad C_V^R(m_b) = 1.07C_V^R(2\text{TeV}), \quad C_S^R(m_b) = 2C_S^R(2\text{TeV}),$$

$$\begin{pmatrix} C_S^L(m_b) \\ C_T(m_b) \end{pmatrix} = \begin{pmatrix} 1.91 & -0.38 \\ 0 & 0.89 \end{pmatrix} \begin{pmatrix} C_S^L(2\text{TeV}) \\ C_T(2\text{TeV}) \end{pmatrix}. \quad (3)$$

A. Analytical Expressions of the Observables

By sandwiching the WEH given in Eq. (1), the analytical expressions of the ratios $R(D^{(*)})$, $R(J/\psi)$ and the observables depend on the polarization of final state particles, $F_L(D^*)$, $P_\tau(D)$ and $P_\tau(D^*)$ can be

parameterized in terms of NP WCs as follows [24, 44, 49, 57, 58, 66, 77, 78, 85, 87]:

$$R(D) = R_D^{SM} \left\{ |1 + C_V^L + C_V^R|^2 + 1.01 |C_S^R + C_S^L|^2 + 1.49 \text{Re} [(1 + C_V^L + C_V^R) (C_S^R + C_S^L)^*] \right. \\ \left. + 0.84 |C_T|^2 + 1.08 \text{Re} [(1 + C_V^L + C_V^R) (C_T)^*] \right\}, \quad (4)$$

$$R(D^*) = R_{D^*}^{SM} \left\{ |1 + C_V^L|^2 + |C_V^R|^2 + 0.04 |C_S^L - C_S^R|^2 + 16.0 |C_T|^2 - 1.83 \text{Re} [(1 + C_V^L) C_V^{R*}] \right. \\ \left. + 6.60 \text{Re} [(C_V^R) C_T^*] - 5.17 \text{Re} [(1 + C_V^L) C_T^*] + 0.11 \text{Re} [(1 + C_V^L - C_V^R) (C_S^R - C_S^L)^*] \right\}, \quad (5)$$

$$F_L(D^*) = F_L(D^*)^{SM} \left(\frac{R_{D^*}}{R_{D^*}^{SM}} \right)^{-1} \left\{ |1 + C_V^L - C_V^R|^2 + 0.08 |C_S^L - C_S^R|^2 + 6.90 |C_T|^2 \right. \\ \left. - 0.25 \text{Re} [(1 + C_V^L - C_V^R) (C_S^L - C_S^R)^*] - 4.30 \text{Re} [(1 + C_V^L - C_V^R) C_T^*] \right\}, \quad (6)$$

$$P_\tau(D^*) = P_\tau(D^*)^{SM} \left(\frac{R_{D^*}}{R_{D^*}^{SM}} \right)^{-1} \left\{ |1 + C_V^L|^2 + |C_V^R|^2 - 0.07 (|C_S^R - C_S^L|^2) - 1.85 |C_T|^2 \right. \\ \left. + 0.23 \text{Re} [(1 + C_V^L - C_V^R) (C_S^L - C_S^R)^*] - 1.79 \text{Re} [(1 + C_V^L) C_V^{R*}] - 3.47 \text{Re} [(1 + C_V^L) C_T^*] \right. \\ \left. + 4.41 \text{Re} [(C_V^R) C_T^*] \right\}, \quad (7)$$

$$P_\tau(D) = P_\tau(D)^{SM} \left(\frac{R_{D^*}}{R_{D^*}^{SM}} \right)^{-1} \left\{ |1 + C_V^L + C_V^R|^2 + 3.04 (|C_S^R + C_S^L|^2) + 0.17 |C_T|^2 \right. \\ \left. + 4.50 \text{Re} [(1 + C_V^L + C_V^R) (C_S^L + C_S^R)^*] - 1.09 \text{Re} [(1 + C_V^L + C_V^R) C_T^*] \right\}, \quad (8)$$

$$R(J/\psi) = R(J/\psi)^{SM} \left\{ |1 + C_V^L|^2 + |C_V^R|^2 - 1.82 \text{Re} [(1 + C_V^L) C_V^{R*}] + 0.04 (|C_S^L - C_S^R|^2) \right. \\ \left. + 0.10 \text{Re} [(1 + C_V^L - C_V^R) (C_S^R - C_S^L)^*] + 14.7 |C_T|^2 - 5.39 \text{Re} [(1 + C_V^L) C_T^*] \right. \\ \left. + 6.57 \text{Re} [(C_V^R) C_T^*] \right\}, \quad (9)$$

$$\mathcal{R}(\Lambda_c) = \mathcal{R}(\Lambda_c)^{SM} \left\{ |1 + C_V^L|^2 + |C_V^R|^2 + 0.491 \text{Re} [(1 + C_V^L) C_S^{R*}] + 0.316 [(1 + C_V^L) C_S^{L*}] \right. \\ \left. + 0.484 [(C_S^L) C_S^{R*}] + 0.31 (|C_S^L|^2 + |C_S^R|^2) - 2.96 \text{Re} [(1 + C_V^L) C_T^*] + 10.52 |C_T|^2 \right. \\ \left. - 0.678 \text{Re} [(1 + C_V^L) C_V^{R*}] + 0.316 \text{Re} [(C_S^R) C_V^{R*}] + 0.491 \text{Re} [(C_S^L) C_V^{R*}] \right. \\ \left. + 4.85 \text{Re} [(C_V^R) C_T^*] \right\}. \quad (10)$$

The ratio $R(X_c)$ of inclusive semileptonic B - meson decays has been discussed in [69], and its expression in terms of NP couplings is

$$R(X_c) = R(X_c)^{SM} \left\{ 1 + 1.147 [|C_V^L|^2 + 2 \text{Re} C_V^L + |C_V^R|^2] - 0.714 \text{Re} [(1 + C_V^L) C_V^{R*}] \right. \\ \left. + 0.031 |C_S^R - C_S^L|^2 + 0.327 |C_S^R + C_S^L|^2 + 12.637 |C_T|^2 + 0.096 [(1 + C_V^L - C_V^R) (C_S^R - C_S^L)^*] \right. \\ \left. + 0.493 [(1 + C_V^L + C_V^R) (C_S^R + C_S^L)^*] + 5.514 \text{Re} [(C_V^R) C_T^*] - 3.402 \text{Re} [(1 + C_V^L) C_T^*] \right\} \quad (11)$$

Similarly, the branching ratio of $B_c \rightarrow \tau \nu$ decay can take the form [10, 56, 59, 60]:

$$\frac{Br(B_c \rightarrow \tau \nu)}{Br(B_c \rightarrow \tau \nu)|_{\text{SM}}} = \left| 1 + (C_V^L - C_V^R) + \frac{m_{B_c}^2}{m_\tau (m_b + m_c)} (C_S^R - C_S^L) \right|^2 \quad (12)$$

B. Fit Procedure

The standard χ^2 analysis of the aforementioned observables for the decays governed by $b \rightarrow c\tau\nu$ transitions can be done by using

$$\chi^2(C_i^X) = \sum_{l,m}^{N_{obs}} \left[O_l^{exp} - O_l^{th}(C_i^X) \right] C_{lm}^{-1} \left[O_m^{exp} - O_m^{th}(C_i^X) \right],$$

where N_{obs} represents the number of observables, $O_l^{exp(th)}$ are the experimental (theoretical) values of the observables, and C_i^X are the NP WCs. C_{lm} is the covariance matrix incorporating the theoretical and experimental uncertainties. However, instead of using covariance matrix, the χ^2 function can be written in the form of pulls, i.e., $\chi^2 = \sum_i^{N_{obs}} \text{pull}_i^2$, where $\text{pull}_i = (O_{\text{exp}}^i - O_{\text{th}}^i) / \sqrt{\sigma_{\text{exp}}^2 + \sigma_{\text{th}}^2}$. Here $\sigma_{\text{exp(th)}}^i$ shows the experimental (theoretical) error which are added in quadrature. The correlation of $R(D)$ and $R(D^*)$ has been taken into account by using the following relation

$$\chi_{R(D)-R(D^*)}^2 = \frac{\text{pull}(R(D))^2 + \text{pull}(R(D^*))^2 - 2\rho\text{pull}(R(D))\text{pull}(R(D^*))}{(1 - \rho^2)}.$$

The latest value of $R(D) - R(D^*)$ correlation reported in ref. [34] is $\rho = -0.37$. For the uncorrelated observables, the value of ρ is zero.

For analysis, using latest data reported by HFLAV (c.f. TABLE I), we first calculate the best fit points by minimizing the χ^2 function (χ_{min}^2) in the region of parameteric space that is compatible with the upper bound of $BR(B_c \rightarrow \tau\nu) < 60\%$, $< 30\%$ and $< 10\%$ [77]. χ_{min}^2 is thus used to evaluate the p-values, which are the measure of goodness of fit and allows us to quantify the level of agreement between the data and the NP scenarios [1, 3, 71]. The number of degrees of freedom (dof), $N_{dof} = N_{obs} - N_{par}$, where $N_{par} = 1(2)$ for 1D (2D) scenarios while number of observables, N_{obs} is the number of observables used in the fitting, i.e., N_{obs} is 4, 6 and 7 for the Fits A, B and C, respectively. The SM Pull is defined as $\text{pull}_{SM} = \chi_{SM}^2 - \chi_{min}^2$, where $\chi_{SM}^2 = \chi^2(0)$, which can be converted into an equivalent significance in units of standard deviations (σ).

C. Specific NP scenarios influenced by Leptoquark (LQ) Models

Among the different NP models, the LQ models have recently gained attention to solve the B -Physics anomalies, therefore, in this study, we consider different 1D and 2D scenarios of LQ models as discussed in refs. [12, 43, 88–132]:

- For 1D scenarios: $C_V^L, C_S^L, C_S^R, C_S^L = 4C_T$,
- For 2D scenarios: $(C_V^L, C_S^L = -4C_T), (C_S^L, C_S^R), (C_V^L, C_S^R), (\text{Re}[C_S^L = 4C_T], \text{Im}[C_S^L = 4C_T])$.

The combinations arise from the C_V^R term will be discussed in the upcoming section separately.

III. ALLOWED PARAMETRIC SPACE IN 1D AND 2D LQ SCENARIOS

In this section, we perform the χ^2 analysis of different 1D and 2D LQ scenarios mentioned above with the latest HFLAV data by using the fitting procedure discussed above.

A. 1D Scenarios

In FIG. (1), we have shown the χ^2 dependence on the WCs for 1D scenarios at 1 and 2 TeV scales of new WC's. The dashed vertical lines correspond to the constraints on C_i^X from the different upper bounds of $BR(B_c \rightarrow \tau\nu)$. The dotted, dashed and solid curves represent the cases of Fits A, B, and C, respectively. From this FIG. 1, one can notice that the positive best fit points of the NP models are not significantly changed with respect to the scales of new WC's, while the negative best fit points and the vertical lines of $BR(B_c \rightarrow \tau\nu)$ are slightly shifted to the right side. It can also be noted from FIG. 1 that the updated data is still indicating that negative solutions of best fit points for C_S^L and C_S^R are still excluded by the maximum upper limit of $BR(B_c \rightarrow \tau\nu) \leq 60\%$ as reported by Blanke *et al.* [1, 3], which is also disfavored with respect to their SM values. One can also see from the plot that near the positive best fit point, the C_V^L and C_S^R still favourable to explain the data, while the favourable situation of C_S^L is further improved with the new data.

In (2-5) columns of TABLE II, we have listed the numerical values of Best fit points, χ_{min}^2 , p-value, $Pull_{SM}$ in different Fits for 1D scenarios where the first, second and third rows represent Fit A, B and C, respectively. The last eight columns show the predictions of different observables at the best fit point with the σ deviation. χ_{SM}^2 and p-value are also given at the top of the table for all Fits. It is worth mentioning here that we have calculated these numerical values on both 1 and 2 TeV scales and found that these values are not significantly changed. It is also clear from TABLE II that except the scenario $C_S^L = 4C_T$, the values of best fit points for all 1D scenarios are almost independent of N_{obs} . Similarly, the slight dependence of best fit point of C_S^R (see TABLE I. of [1]) on $BR(B_c \rightarrow \tau\nu)$ is also disappeared for the new data. The p-values, $Pull_{SM}$ and predictions of different observables for 1D scenarios are also tabulated in TABLE II. The 1σ and 2σ intervals for WCs have also been calculated and are listed in TABLE V. One can see that the p-values for all 1D scenarios are improved by considering the new experimental data, particularly, for C_V^L (C_S^R). These two scenarios are significantly enhanced and moved up to 43.2% (12.9%) for the Fit A ($N_{obs} = 4$) which previously found to be 35% ($\simeq 2\%$) [1]. This shows that C_V^L (C_S^R) are still favorable and although the p-value of $C_S^L = 4C_T = (0.06 - 0.1)\%$ slightly improved but this scenario still describes the data poorly.

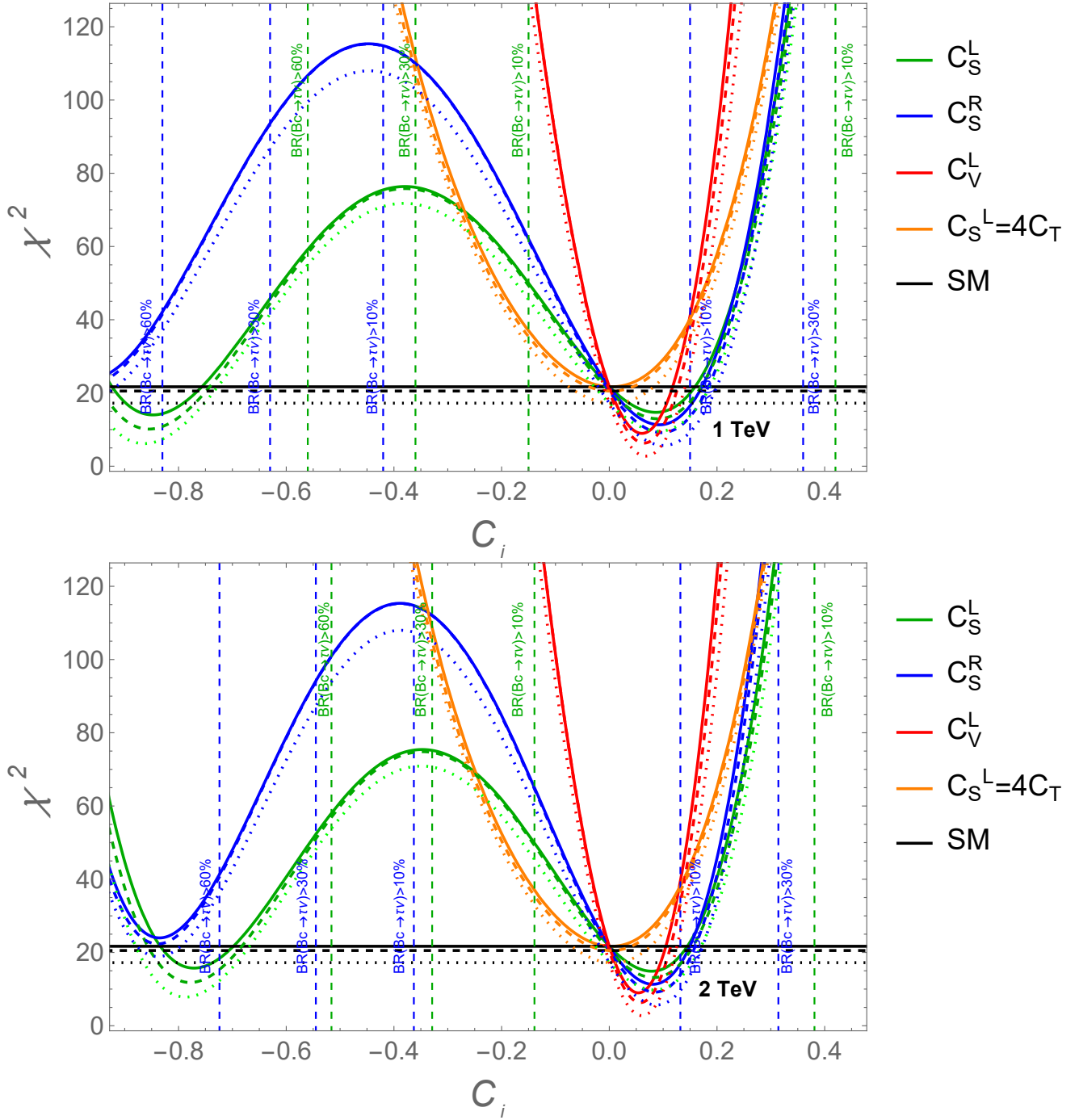


FIG. 1: Dependence of χ^2 with one Wilson coefficient active at a time for different Fits at 1 and 2 TeV scales. The colored dotted, dashed and solid lines represent Fits A, B and C, respectively, while the black lines represent their SM values. The dashed vertical lines correspond to the constraint for $C_S^{L,R}$ from $B_c \rightarrow \tau\nu$ assuming the values of 10% and 30% and 60%.

We can see from TABLE II that with increasing the number of observables, χ_{min}^2 (p-value) is increased (decreased), consequently, the pull is reduced with all Fit cases under consideration except C_V^R . This translates that p-value decreases except for the scenarios $(C_S^L, C_S^L = 4C_T)$, when we include the data of

observables $R(J/\psi)$ and $R(\Lambda_c)$ in the analysis reducing the goodness of fit. This is attributed to the large experimental uncertainty in the measurement of $R(J/\psi)$ and inconsistency of the measurement of $R(\Lambda_c)$ with respect to $R(D^{(*)})$.

$$\chi_{SM}^2 = (17.22, 20.52, 21.69)_{A,B,C}, p - value = (1.75, 2.23, 2.86)_{A,B,C} \times 10^{-3},$$

Scenarios	Best fit	χ_{min}^2	$p - value\%$	$pull_{SM}$	$R(D)$	$R(D^*)$	$R(J/\psi)$	$F_L(D^*)$	$P_\tau(D^*)$	$P_\tau(D)$	$R(X_c)$	$R(\Lambda_c)$
C_S^L		9.76	2.07	2.73								
	0.08	13.15	2.20	2.71	0.372 0.52σ	0.249 -2.91σ	0.254 -1.84σ	0.454 -1.63σ	-0.521 -0.25σ	0.517	0.230 0.23σ	0.341 1.30σ
		14.88	2.12	2.60								
C_S^R	0.09	5.66	12.9	3.40								
	0.08	9.17	10.2	3.36	0.387 1.03σ	0.259 -2.08σ	0.262 -1.81σ	0.476 -1.38σ	-0.465 -0.15σ	0.559	0.241 0.5σ	0.351 1.44σ
	0.08	11.31	7.9	3.22								
C_V^L	0.06	2.75	43.2	3.80								
	0.06	6.31	27.7	3.76	0.339 -0.62σ	0.289 0.42σ	0.293 -1.68σ	0.464 -1.52σ	-0.497 -0.21σ	0.331	0.250 0.78σ	0.364 1.61σ
	0.05	8.96	17.5	3.56								
C_V^R		14.18	0.3	1.76								
	-0.05	17.16	0.4	1.84	0.266 -3.13σ	0.279 -0.42σ	0.283 -1.72σ	0.467 -1.49σ	-0.496 -0.21σ	0.331	0.226 0.1σ	0.335 1.22σ
		18.60	0.5	1.75								
$C_S^L = 4C_T$	0.007	17.17	0.06	0.22								
	0.004	20.51	0.09	0.14	0.301 -1.93σ	0.252 -2.66σ	0.256 -1.83σ	0.463 -1.53σ	-0.498 -0.22σ	0.337	0.215 -0.27σ	0.323 1.07σ
	0.004	21.67	0.1	0.13								

TABLE II: Fit results for 1D scenarios by using all available data: Best fit points, χ_{min}^2 , p-value, $Pull_{SM}$ are given. The columns (2-5) represent the results for different parameters: First, second and third rows represent Fit A, B and C, respectively. The last eight columns show the predictions of different observables at the best fit point with the σ deviation. χ_{SM}^2 and p-value are also given at the top of the table for all Fits.

For the best fit points of the NP scenario the theoretically predicted values of the observables are given in TABLE II. Using the relation [1]

$$d_{O_i} = \frac{O_i^{NP} - O_i^{exp}}{\sigma O_i^{exp}} \quad (13)$$

here we have also given their discrepancies from the corresponding experimental values. The results can be concluded from the above table as: For $R(D)$, $P_\tau(D^*)$ and $R(X_c)$, the deviations are found to be less than 1σ for all NP scenarios except $R(D)$ in $C_S^L = 4C_T$ (C_V^R) scenario, where it is found to be -1.93σ (-3.13σ). On the other hand, for the observables, $R(D^*)$, $R(J/\psi)$, $F_L(D^*)$ and $R(\Lambda_c)$, the deviations are between $1 - 3\sigma$, except for $R(D^*)$ in C_V^L which is 0.42σ . It is also important to mention here that the values of these observables are mildly effected by changing N_{obs} in the analysis.

B. 2D scenarios

In this section, we will perform the phenomenological analysis of 2D NP scenarios that are defined in section II C, which are generated by exchanging a single new LQ or Higgs particle. In this case, for the χ^2 analysis, we have considered $N_{par} = 2$.

In FIG. 2, we have plotted the 1σ and 2σ allowed parametric space in the 2D NP scenarios planes. The shaded colored regions (the black contours) represent at 2 TeV (1 TeV) allowed parametric space for the Fit A, while the solid red and dashed contours are for Fits B and C, respectively. Moreover in FIG. 2, for the comparison with ref. [1], we have also shown the allowed parametric regions by the blue contours for NP scenarios for Fit A where the authors of ref. [1] considered the old data of the observables. The gray hatched regions are excluded by the 60% and 10% upper limits on the branching ratio $B_c \rightarrow \tau\nu$. From the plots of FIG. 2, one can easily see that how the allowed parametric space is changed by changing the scale of NP WC's from 1 TeV to 2 TeV and by the updated data. One can observe that the updated data and shifting the scale of NP WC's from low to high, squeeze the allowed parametric space of NP scenarios.

It can be noted from FIG. 2a that the allowed parametric space for scenario $(C_V^L, C_S^L = -4C_T)$ for Fit A (orange shaded region) is not much effected whether we include the $R(J/\psi)$ (Fit B (red solid contour)) or by inclusion of $R(J/\psi)$ and $R(\Lambda_c)$ together (Fit C (red dashed contour)) in the analysis. On the other hand, the scenario (C_V^L, C_S^R) , the allowed parametric space is neither effected by the $B_c \rightarrow \tau\nu$ nor by the number of observables and remained approximately same for Fit A, B and C. FIGS. 2c and 2d depict the allowed parametric space for scenarios (C_S^L, C_S^R) and $(\text{Re}[C_S^L = 4C_T], \text{Im}[C_S^L = 4C_T])$, respectively, where red (green) shaded region represents with $B_c \rightarrow \tau\nu \leq 60\%$ ($\leq 10\%$). From these figures, one can see that for both these scenarios the allowed parametric space at $B_c \rightarrow \tau\nu \leq 10\%$ are almost remain the same for Fits A, B and C. On the other hand at $B_c \rightarrow \tau\nu \leq 60\%$, the parametric space get elongated for Fit C (red dashed contour).

By applying the upper limits of $BR(B_c \rightarrow \tau\nu) < 60\%$, $< 30\%$ and $< 10\%$, the results for the different parameters of 2D scenarios for the Fits A, B and C are given in TABLE III. One can observe that for all the fitting cases, the best fit point of scenarios $(C_V^L, C_S^L = -4C_T)$ and (C_V^L, C_S^R) are not effected by the $BR(B_c \rightarrow \tau\nu)$, where as it is not the case for the other two scenarios, (C_S^L, C_S^R) and $(\text{Re}[C_S^L = 4C_T], \text{Im}[C_S^L = 4C_T])$ as mentioned in [1] also. However, by using the updated data for Fit A, the goodness of the fit (p-value) increases $\sim 4\%$ ($22\% \rightarrow 26.1\%$) for $(C_V^L, C_S^L = -4C_T)$ and $\sim 2\%$ ($30.8\% \rightarrow 32.9\%$) for (C_V^L, C_S^R) . Here, one can also notice from FIG. 2c that the NP scenario (C_S^L, C_S^R) is significantly effected by the WC's scale as compared to other three scenarios. Therefore, for (C_S^L, C_S^R) by setting $BR(B_c \rightarrow \tau\nu) < (10, 30, 60)\%$ the p-values are increased $\sim (10, 36, 3)\%$ at 2 TeV and $\sim (9, 28, 7)\%$ at 1 TeV, respectively.

Therefore, the updated data indicate that the scenario (C_S^L, C_S^R) with hard cut $BR(B_c \rightarrow \tau\nu) < 30\%$ is also looking favorable. The variation in p-value for the scenario $(\text{Re}[C_S^L = 4C_T], \text{Im}[C_S^L = 4C_T])$ is also

improved, as for $BR(B_c \rightarrow \tau\nu) < 60\%$ and $< 30\%$, the p-value is increased from $22\% \rightarrow 25.9\%$ while for $BR(B_c \rightarrow \tau\nu) < 10\%$, the p-value is increased from $0.3\% \rightarrow 11\%$. Hence, the latest data is showing that the impact of $BR(B_c \rightarrow \tau\nu)$ on the p-values is become more crucial, therefore, an accurate measurement of $BR(B_c \rightarrow \tau\nu)$ will be helpful to clear the smog for the most favourable NP scenario.

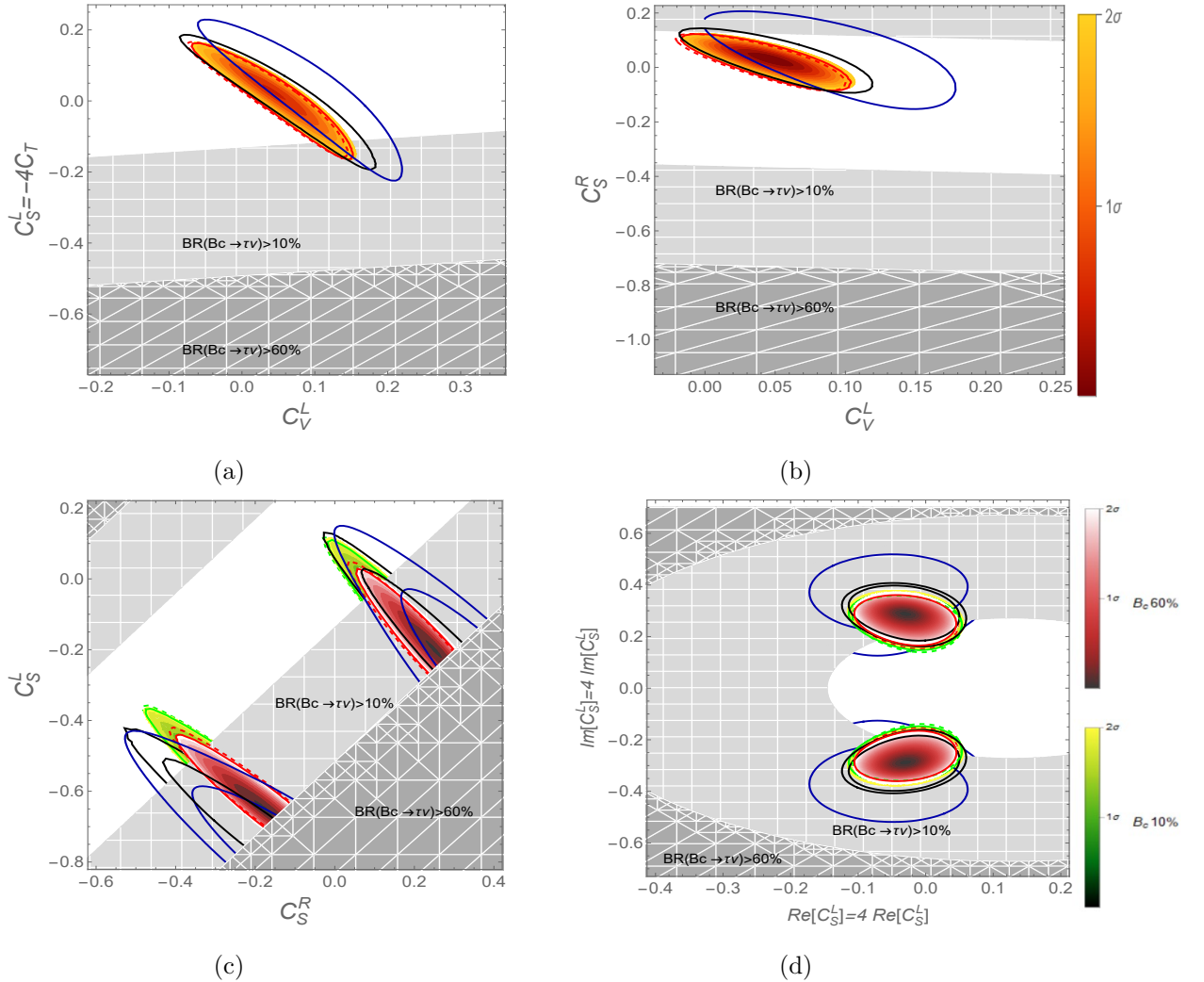


FIG. 2: Results of the fits for 2D NP scenarios. The light and dark gray regions show the 10% and 60% branching ratio constraints. The light (dark) shaded contours represent the 1σ (2σ) intervals. Figs. (a), (b), (c) and (d) show the $(C_V^L, C_S^L = -4C_T)$, (C_V^L, C_S^R) , (C_S^R, C_S^L) and $(Re[C_S^L] = 4C_T, Im[C_S^L] = 4C_T)$ scenarios, respectively. The shaded contours represent Fit A, solid contours represent Fit B and the dashed contours represent Fit C. The shaded contours represent Fit A, solid contours represent Fit B and the dashed contours represent Fit C. The red and green colors in Figs. 1c and 1d show the allowed parametric region when the branching ratio constraints are taken to be 60% and 10%, respectively. The blue (black) contours show the results by using the previous (new) data of $R(D^{(*)})$ at 1TeV.

Apart from the dependence of $BR(B_c \rightarrow \tau\nu)$, we also analyze the impact of N_{obs} on the parameters of NP scenarios. For this purpose, we compare the values of different parameters of Fits A, B and C, which are listed in TABLE III. It is also important to mention here that the experimental value of $R(X_c)$ lies

within its SM predicted value and does not significantly effect the parameters of NP scenarios. In contrast to it, the data of $R(J/\psi)$ and $R(\Lambda_c)$ directly effect the parametric space of NP scenarios as can be seen from the given values of different parameters in TABLE III. These values show that the goodness of fit (the p-value) is decreased when we increased the N_{obs} . For instance, the p-value of most favorable scenario (C_S^L, C_S^R) at $BR(B_c \rightarrow \tau\nu) < 60\%$ is 71% for Fit A is reduced up to 37% for Fit B (the case, when we include the $R(J/\psi)$ observable in the analysis) and even further reduced for Fit C (the case, when we added both $R(J/\psi)$ and $R(\Lambda_c)$ observables) and remained 21.72% only.

- Interestingly, for Fit C, at $BR(B_c \rightarrow \tau\nu) < 10\%$, the most favorable scenario (C_S^L, C_S^R) becomes less favorable ($p - value = 6.87$) in comparison with some other NP scenarios, as we can see from the p-values given in TABLE III. Although, there is a large uncertainty in the experimental value of $R(J/\psi)$ and similarly, the recent experimental measurement of $R(\Lambda_c)$ is under debate [2], the behavior of analysis that discussed above is indicating that the future data on different observables is also valuable to decide which NP scenario is more suitable to explain the various anomalies.

$$\chi_{SM}^2 = (17.22, 20.52, 21.69)_{A,B,C}, p - value = (1.75, 2.23, 2.86)_{A,B,C} \times 10^{-3},$$

Scenarios	Best fit	χ_{min}^2	P-Value%	$pull_{SM}$	$R(D)$	$R(D^*)$	$R(J/\psi)$	$F_L(D^*)$	$P_\tau(D^*)$	$P_\tau(D)$	$R(X_c)$	$R(\Lambda_c)$
$(C_V^L, C_S^L = -4C_T)$	(0.04,0.03)	2.61	26.11	3.81								
		6.17	17.82	3.78	0.352 -0.17σ	0.285 0.08σ	0.289 -1.70σ	0.457 -1.59σ	-0.500 -0.22σ	0.403	0.249 0.86σ	0.367 1.65σ
		8.77	11.11	3.59								
$(C_S^L, C_S^R)_{60\%}$	(-0.65,-0.18),(-0.19,0.25) (-0.64,-0.18),(-0.19,0.24) (-0.62,-0.19),(-0.18,0.22)	0.70	70.4	4.06								
		4.24	37.4	4.05	0.334 -0.79σ	0.283 -0.08σ	0.285 -1.72σ	0.521 -0.88σ	-0.343 0.07σ	0.439	0.243 0.67σ	0.368 1.66σ
		7.18	21.72	3.80								
$(C_S^L, C_S^R)_{30\%}$	(-0.58,-0.24),(-0.13,0.19)	1.46	48	3.96								
		4.87	30.1	3.95	0.361 0.14σ	0.275 -0.75σ	0.278 -1.74σ	0.508 -1.02σ	-0.379 0.001σ	0.487	0.246 0σ	0.364 1.61σ
		7.53	18.4	3.76								
$(C_S^L, C_S^R)_{10\%}$	(-0.49,-0.34),(-0.03,0.10)	4.58	10.2	3.55								
		7.91	9	3.53	0.366 0.31σ	0.261 -1.91σ	0.265 -1.79σ	0.481 -1.33σ	-0.451 -0.13σ	0.502	0.234 0.37σ	0.370 1.68σ
		10.24	6.87	3.39								
(C_V^L, C_S^R)	(0.05,0.03) (0.05,0.03) (0.04,0.03)	2.22	32.9	3.87								
		5.89	20.74	3.82	0.361 -0.14σ	0.285 0.08σ	0.289 -1.70σ	0.467 -1.48σ	-0.487 -0.19σ	0.392	0.252 0.96σ	0.371 1.70σ
		8.53	12.9	3.62								
$(Re[C_S^L = 4C_T], Im[C_S^L = 4C_T])_{60\%,30\%}$	(-0.03,±0.29) (-0.03,±0.28) (-0.03,±0.27)	2.68	25.86	3.81								
		6.23	17.7	3.78	0.357 0σ	0.284 0σ	0.287 -1.70σ	0.453 -1.64σ	-0.436 -0.11σ	0.962	0.249 0.87σ	0.367 1.65σ
		8.79	11.2	3.59								
$(Re[C_S^L = 4C_T], Im[C_S^L = 4C_T])_{10\%}$	(-0.01,±0.24)	4.31	11	3.59								
		7.60	10.4	3.58	0.347 -0.34σ	0.270 -1.17σ	0.274 -1.76σ	0.456 -1.60σ	-0.458 -0.14σ	0.840	0.238 0.5σ	0.353 1.46σ
		9.71	8	3.46								

TABLE III: Fit results for 2D scenarios at 2TeV, including all available data: Best fit points, χ_{min}^2 , p-value, $Pull_{SM}$ are given. The columns (2-5) represent the results for different parameters: First, second and third rows represent Fit A, B and C, respectively. The last eight columns show the predictions of different observables at the best fit point with the σ deviation.

1. Discussion about C_V^R related scenarios

In this section, we will discuss the possible scenarios associated with C_V^R , i.e., (C_V^L, C_V^R) , (C_S^L, C_V^R) , (C_S^R, C_V^R) and $(C_V^R, C_S^L = 4C_T)$, where the last one is related with the R_2 model [66]. The corresponding plots are drawn in FIG. 3, with shaded brown, solid red and dashed red contours representing the cases Fits A, B and C, respectively, at 2 TeV while the black contours are at 1 TeV. It can be seen that these scenarios are independent of branching ratio constraints with the exception that the scenario (C_S^R, C_V^R) is slightly effected by 10% branching ratio constraint. Moreover, the 1σ , 2σ allowed parametric space, and the best fit points of these scenarios are not significantly effected after including $R(J/\psi)$ (Fit B, solid red contour) and $R(\Lambda_c)$ (Fit C, dashed red contour) in the analysis. The p-values and the other parameters of these scenarios are reported in the TABLE IV. The trend and the variation in the values of χ^2 , pull and p-value with respect to the N_{obs} show that the scenario (C_S^R, C_V^R) is most favorable among the other scenarios for Fit A while for Fit B the scenarios (C_S^R, C_V^R) and $(C_V^R, C_S^L = 4C_T)$ both are equally likely. However, to explore more about the NP scenarios, as mentioned in previous section, the theoretical prediction of $R(J/\psi)$ and the experimental measurement of $R(\Lambda_c)$ required further precision.

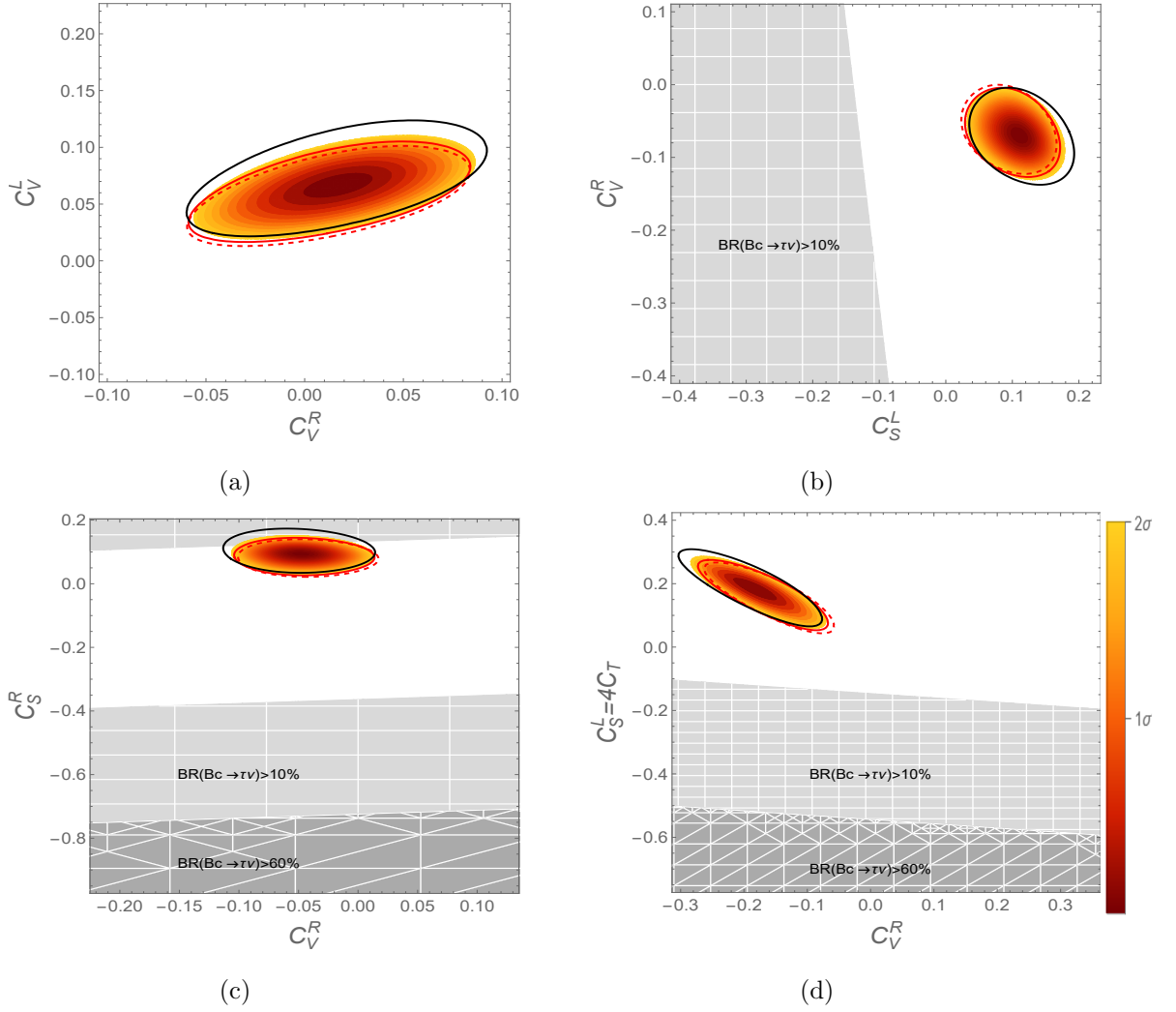


FIG. 3: Results of the fits for the 2D C_V^R scenarios (a) (C_V^L, C_V^R) , (b) (C_S^L, C_V^R) , (c) (C_V^R, C_S^R) and (d) $(C_V^R, C_S^L = 4C_T)$. The shaded contours represent Fit A, solid contours represent Fit B and the dashed contours represent Fit C. The gray portion represents the excluded regions by the 60% and 10% upper limits on branching ratio $B_c \rightarrow \tau\nu$. The black contours show the allowed parametric space at 1 TeV.

$$\chi_{SM}^2 = (17.22, 20.52, 21.69)_{A,B,C}, p - value = (1.75, 2.23, 2.86)_{A,B,C} \times 10^{-3},$$

Scenarios	Best fit	χ_{min}^2	$p - value\%$	$pull_{SM}$	$R(D)$	$R(D^*)$	$R(J/\psi)$	$F_L(D^*)$	$P_\tau(D^*)$	$P_\tau(D)$	$R(X_c)$	$R(\Lambda_c)$
(C_V^L, C_V^R)	(-0.91,-1.)	2.40	30.11	3.84								
		6.06	19.4	3.80	0.353 -0.14σ	0.281 -0.25σ	0.285 -1.71σ	0.462 -1.53σ	-0.497 -0.21σ	0.331	0.248 0.9σ	0.366 1.63σ
		8.73	12.0	3.60								
(C_S^L, C_V^R)	(0.11,-0.07)	2.64	26.7	3.81								
		6.14	18.8	3.79	0.354 -0.10σ	0.284 0σ	0.289 -1.70σ	0.456 -1.60σ	-0.524 -0.26σ	0.615	0.248 0.83σ	0.365 1.62σ
		8.67	12.3	3.60								
(C_S^R, C_V^R)	(0.09,-0.05)	1.83	40	3.92								
		5.44	24.5	3.88	0.352 -0.17σ	0.285 -0.083σ	0.289 -1.70σ	0.479 -1.35σ	-0.465 -0.15σ	0.563	0.249 0.86σ	0.367 1.64σ
		8.07	15.2	3.69								
$(C_V^R, C_S^L = 4C_T)$	(-0.18,0.18)	2.14	34.3	3.88								
		5.74	21.9	3.84	0.354 -0.10σ	0.284 0σ	0.286 -1.71σ	0.472 -1.43σ	-0.572 -0.34σ	0.801	0.248 0.83σ	0.367 1.64σ
		8.36	13.7	3.65								

TABLE IV: The Best fit point, χ_{min}^2 , p-value and $Pull_{SM}$ of 2D scenarios related to C_V^R at 2 TeV are given in the columns (2-5). First row represents Fit A, second row represents Fit B and last row shows Fit C. Last eight columns shows the predictions of different observables at the best fit point with the sigma deviation.

IV. SUM RULE AND CORRELATION OF OBSERVABLES

In this section, we have calculated and analyzed the correlation among different observables in 2D scenarios under consideration - but before that we want to validate the sum rule among the observables $R(D^{(*)})$ and $R(\Lambda_c)$ given in refs. [1-3]. We can see that by using the Eqs. (4, 5, 10), the sum rule reads as

$$\frac{R(\Lambda_c)}{R_{SM}(\Lambda_c)} = 0.276 \frac{R(D)}{R_{SM}(D)} + 0.724 \frac{R(D^*)}{R_{SM}(D^*)} + x_1 \quad (14)$$

where one can see that even with the different analytical expressions of $R(D^{(*)})$, the coefficients of first two terms on the right hand side in the above equation are almost similar to the ref. [2]. The only change appears in the remainder x_1 , which in our case becomes

$$x_1 = -Re \left[(1 + C_V^L) \left(0.122 (C_T)^* + 0.019 (C_S^L)^* + 0.132 (C_V^R)^* \right) \right] + Re[(C_V^R)^*] (0.018 C_S^R + 0.351 C_T). \quad (15)$$

The values of x_1 for 1D [2D] scenarios are 10^{-5} [10^{-3}] and the updated predicted value of $R(\Lambda_c)$ by using the latest data of $R(D^{(*)})$ [34] is

$$\begin{aligned} R(\Lambda_c) &= R_{SM}(\Lambda_c) (1.140 \pm 0.041) \\ &= 0.369 \pm 0.013 \pm 0.005, \end{aligned} \quad (16)$$

which is not significantly different from the numbers reported in [2]. This shows that the latest data of $R(D^{(*)})$ again confirms the validity of the above sum rule. In Eq. (16), the first and the second errors come

from the experimental and form factors uncertainties, respectively. However, the current experimentally measured value of $R(\Lambda_c)$ is larger than the predicted value by sum rule as well as inconsistent with the $R(D^{(*)})$ data pattern and need further future experimental confirmation as discussed in ref. [2].

In addition, the latest predicted SM value of the observable $R(J/\psi) = 0.258 \pm 0.038$ [68], is smaller than its experimentally measured value: $0.71 \pm 0.17 \pm 0.18$ [2, 18], which shows the same behavior as $R(\Lambda_c)$, i.e. deficit in taus in contrast of $R(D^{(*)})$ data. Therefore, it is also interesting to find out the sum rule of $R(J/\psi)$ in terms of $R(D^{(*)})$, which we have derived by using the Eqs. (4, 5, 9) as follows:

$$\frac{R(J/\psi)}{R_{SM}(J/\psi)} = 0.006 \frac{R(D)}{R_{SM}(D)} + 0.994 \frac{R(D^*)}{R_{SM}(D^*)} + x_2, \quad (17)$$

where

$$x_2 = -Re \left[(1 + C_V^L) \left(0.019 C_S^{R*} + 0.257 C_T^* + 0.013 C_V^{R*} - 0.0004 C_S^{L*} \right) \right] + 0.006 \left(|C_R^S|^2 + |C_L^S|^2 \right) \\ + 0.013 Re [C_S^L C_S^{R*}] - 1.205 |C_T|^2 - Re [C_V^{R*}] [0.018 C_S^L - 0.0031 C_T - 0.004 C_S^R].$$

and the remainder x_2 for this observable in 1D [2D] scenarios are 10^{-5} [10^{-3}]. The predicted value of $R(J/\psi)$ by using the above sum rule is

$$R(J/\psi) = R_{SM}(J/\psi) (1.119 \pm 0.046) \\ = 0.289 \pm 0.013 \pm 0.043. \quad (18)$$

One can see that both the SM value of $R(J/\psi)$ as well as its predicted value obtained by sum rule using updated data are smaller than its experimental value and follow the coherent pattern as in the $R(D^{(*)})$ case, i.e. abundance of taus in comparison of light leptons. But in case of $R(J/\psi)$, even though its tensor form factors are not precisely calculated yet, the theoretical predicted values are quite smaller in comparison of its experimental value with large uncertainties, $0.71 \pm 0.18 \pm 0.17$, and suggests that this value also need the further experimental confirmation.

It will be interesting to see how the the updated data change the correlation among the $R(D^{(*)})$, $R(\Lambda_c)$, $F_L(D^*)$ and $P_\tau(D^{(*)})$ observables which are calculated in [1], and for that the updated and the previous results are shown in FIG. 4 by using 1σ parametric range of 2D scenarios. It is worth mentioning here that these correlations are significantly effected by considering the updated values of $R(D^{(*)})$ while the inclusion of $R(J/\psi)$ and the recently measured $R(\Lambda_c)$ data mildly effect the behavior of correlations. However, to see their effects explicitly, we have also shown the correlations of 1σ parametric space of Fit-A (un-filled region) and Fit-C (filled region) in FIG. 4. In addition, to see the effects by the scale of WC's on the correlations, we have also calculated these correlations at 1 TeV for Fit A and shown by the black curves. As mentioned above in section III-B that the updated values of $R(D^{(*)})$ squeezed the parametric space of 2D scenarios significantly (see FIG. 2). Consequently, it shrink and lower the values of correlation regions among the observables $R(D^{(*)})$ and $R(\Lambda_c)$, which is more close to the SM values of these observables as can be seen from the first four plots of Fig. 4. Similarly, the changes by the updated data of $R(D^{(*)})$ in the

correlation regions among the observables $P_\tau(D^{(*)})$ and $F_L(D^*)$ are depicted in plots five to ten of FIG. 4. In addition, the correlations among $R(D^{(*)})$, $R(X_c)$ $R(J/\psi)$ are also shown in last eight plots of FIG. 4. On the other hand, for the scenarios related to C_V^R , the correlation among the observables by using the 1σ parametric space are plotted in FIG. 5.

Finally, from Eq. (13), the predicted values of observables used in fitting analysis are also calculated by using the 1σ parametric space of the 2D NP scenarios and listed them in TABLES III and IV. It can be seen that the predicted values of $R(D^{(*)})$, $P_\tau(D^*)$ and $R(X_c)$ show less than 1σ deviations except for the scenarios ($Re[C_S^L = 4C_T]$, $Im[C_S^L = 4C_T]$) and (C_S^L, C_S^R) for 10% branching ratio. However, the observables $R(J/\psi)$ and $F_L(D^*)$ exhibit 2σ deviation except the scenario (C_S^L, C_S^R) for 60% branching ratio. Similarly, the predicted value of $\mathcal{R}(\Lambda_c)$ is showing approximately 2σ deviation with respect to its experimentally measured numbers.

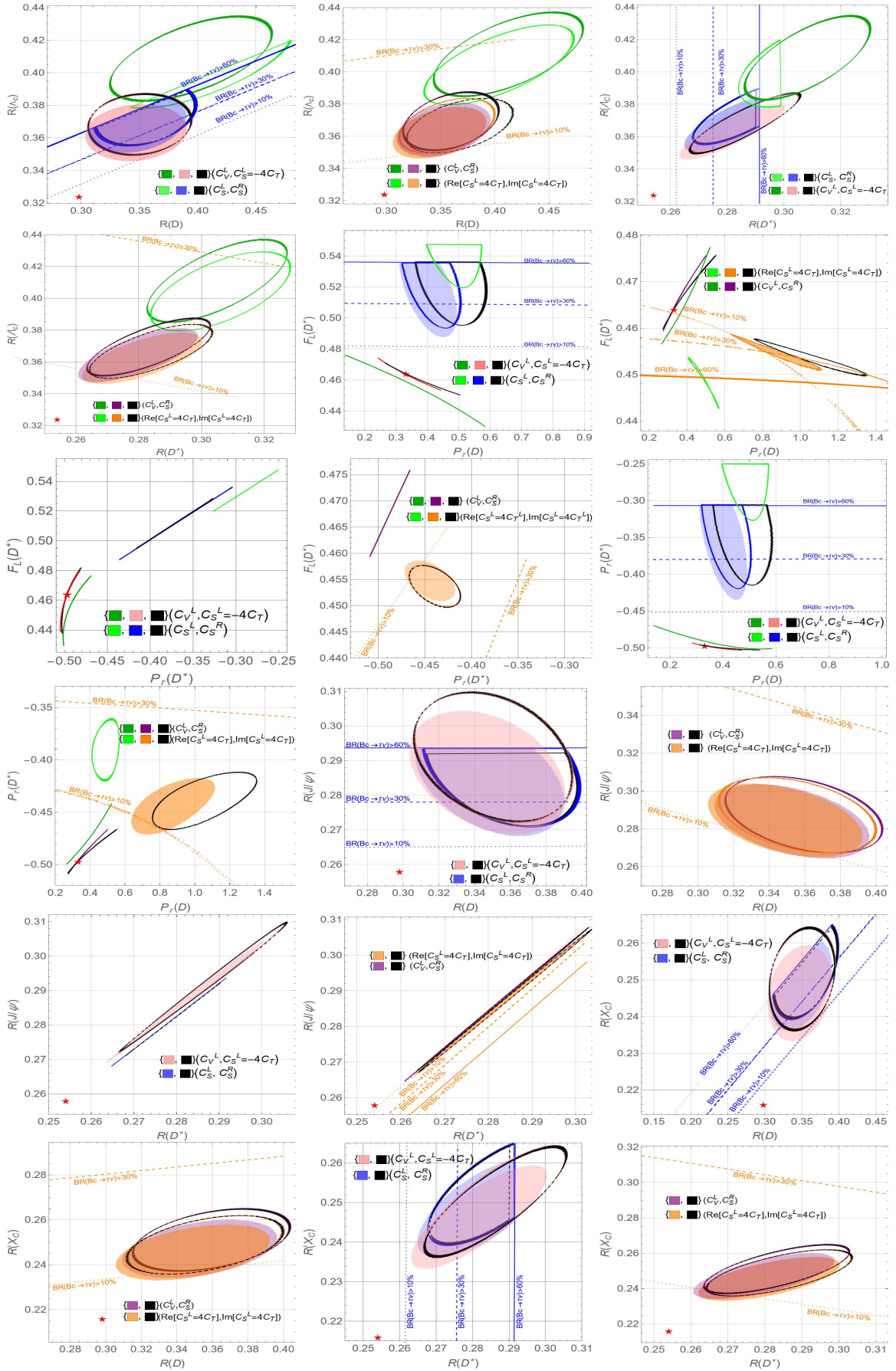


FIG. 4: Correlations plots for preferred 1σ regions with the $BR(B_c \rightarrow \tau\nu) < 60\%$. The green (black) contours represent the plots of ref. [1] at 1 TeV while filled (unfilled) contours represent Fit C (A). The solid, dashed and dotted lines refer to constraints on $BR(B_c \rightarrow \tau\nu)$ (60, 30, 10)%, respectively. SM predictions are represented by red star.

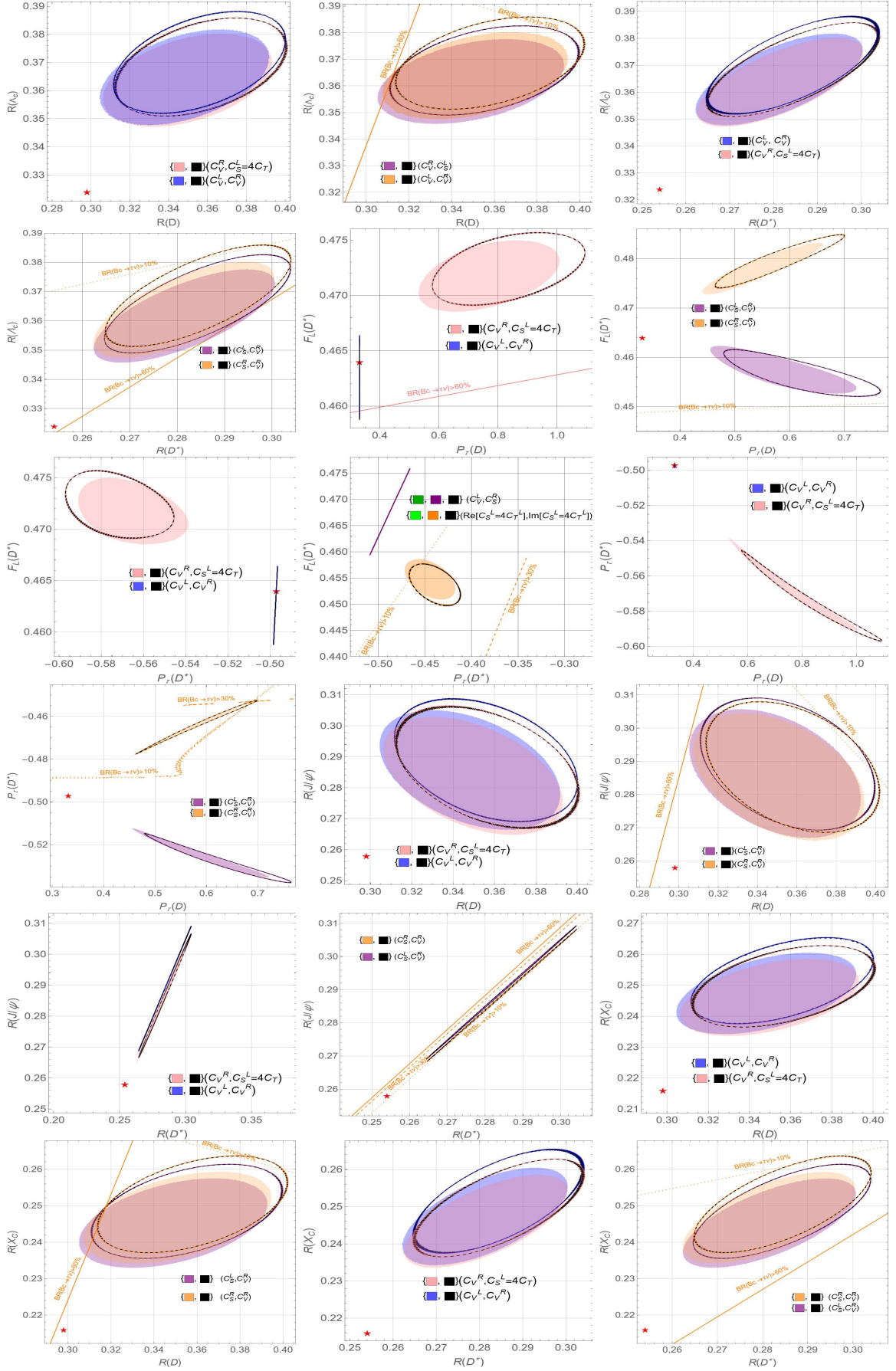


FIG. 5: The legends are same as described in FIG. 4 but for C_V^R related scenarios.

V. SENSITIVITY OF ANGULAR OBSERVABLES TO NEW PHYSICS (NP)

For the NP point of view, it is important to mention here that the form factors are the main source of hadronic uncertainties, consequently, generate the errors in the theoretical predictions which may preclude the effects of NP. Therefore, we need to select those observables which are not only sensitive to NP but also the variation in their values in the presence of NP may provide a discriminatory tool among the different NP scenarios.

To accomplish this purpose, we have considered the lepton forward-backward asymmetry (A_{FB}^ℓ), the forward-backward asymmetry of transversely polarized D^* meson ($A_{FB}^{T,L}$), the longitudinal polarization fraction of the D^* meson ($F_L(D^*)$), the ratios ($R_{A,B}$, $R_{L,T}$), and the angular asymmetries: A_3 , A_4 , A_5 , A_{6s} for the decay channel $B \rightarrow D^* \tau \nu_\tau$ which are relatively clean and also sensitive to the NP. Therefore, the variation in their values in the presence of 1D and 2D NP scenarios (under consideration) could be used to discriminate these NP scenarios. These CP-even angular observables are discussed in detail in the literature and their analytical expressions in terms of angular coefficients, I 's, can be found in [45, 74, 134]. Furthermore, in the current study, we rely on the form factors which are calculated in ref. [45, 134] and observables mentioned above have been presented with their theoretical uncertainties.

To see the sensitivity of these angular observables to NP, we have plotted them against the square of transverse momentum, q^2 , in Figs. 6 and 8 for 1D and 2D NP scenarios, respectively. In these figures, the black band shows the SM values of these observables where the width corresponds to the uncertainty in the values due to the form factors. The color bands represent their values in the presence of NP. For the NP dependence of these observables, we have used the central values of the form factors and the width of light and dark color bands show the uncertainty due to 1σ and 2σ intervals in the NP WCs at 2 TeV, respectively. The effects of different 1D and 2D NP scenarios on the above mentioned angular observables are discussed in the following sections. In addition, to see the direct influence of the scenarios on observables, we have also found the expressions I 's in terms of NP WCs, $C_i^{L(R)}$, after integrating q^2 and these are given in Appendix.

One can immediately see that the expressions of coefficients I 's in terms of NP WCs make the study of NP in different angular observables quite trivial. Therefore, by using these expressions of I 's, we have calculated the variation in the amplitude of different angular observables in the presence of NP and shown by the bar plots in FIGS. 7 and 9 for 1D and 2D NP scenarios, respectively. The corresponding SM predictions and values at different scenarios are also listed in Tables VI and VII, respectively.

As we have mentioned above in III that for the scenarios: $(C_V^L, C_S^L = -4C_T)$, (C_V^L, C_S^R) , the allowed parametric space of NP does not significantly change by the number of observables and the branching ratio constraints, while the allowed parametric space of the scenarios: $(Re[C_S^L = 4C_T], Im[C_S^L = 4C_T])$, (C_S^L, C_S^R) are effected only by the branching ratio constraints. It is worth mentioning here that we have found the allowed 1σ and 2σ parametric space for the Fit A, B and C, are almost same. However, to see

the impact of NP effects on the numerical values of angular observables, we use the 1σ and 2σ parametric space with the 60% branching ratio that are given in Table V.

1D Scenarios	1σ interval	2σ interval	2D Scenarios	1σ interval	2σ interval
C_S^L	(0.05,0.10)	(0.02,0.13)	$(C_V^L, C_S^L = -4C_T)$	$(0.01,0.06)\epsilon C_V^L$ $(-0.003,0.06)\epsilon C_S^L$	$(-0.003,0.07)\epsilon C_V^L$ $(-0.03,0.08)\epsilon C_S^L$
C_S^R	(0.06,0.10)	(0.03,0.12)	(C_S^L, C_S^R)	$(-0.74,-0.65)\epsilon C_S^L$ $(-0.25,-0.15)\epsilon C_S^R$	$(-0.76,-0.63)\epsilon C_S^L$ $(-0.28,-0.11)\epsilon C_S^R$
C_V^L	(0.04,0.07)	(0.02,0.08)	(C_V^L, C_S^R)	$(0.02,0.07)\epsilon C_V^L$ $(-0.01,0.07)\epsilon C_S^R$	$(0.004,0.09)\epsilon C_V^L$ $(-0.05,0.09)\epsilon C_S^R$
$C_S^L = 4C_T$	(-0.03,0.03)	(-0.07,0.07)	$(Re[C_S^L = 4C_T], Im[C_S^L = 4C_T])$	$(-0.07,0.02)\epsilon RC_S^L$ $(-0.32,0.32)\epsilon ImC_S^L$	$(-0.10,0.05)\epsilon RC_S^L$ $(-0.35,0.35)\epsilon ImC_S^L$

TABLE V: 1σ and 2σ allowed parametric space by using the 60% branching ratio for 1D and 2D scenarios.

A. Effects of 1D scenarios on observables

The sensitivity of different angular observables by taking one of the NP WCs, $C_i^{(L,R)}$, is set to be non zero and are plotted in FIG. 6. One can see that the values of all angular observables are significantly effected by the NP scenario: $C_S^L = 4C_T$ except the observables $R_{L,T}$ and $F_L(D^*)$ while the other 1D scenarios have, comparatively, mild effects or rather their effects are preclude by the uncertainties. Furthermore, one can see from FIG. 6, the effects of NP scenario: $C_S^L = 4C_T$ on the angular observables is more prominent at low [middle, high] q^2 for A_5, A_{FB}^T [$(A_6^s, R_{A,B}, C_L^F), (A_3, A_4, A_{FB}^L)$]. Therefore, the bin wise precise measurements of the observables are also important to probe the NP and to distinguish among different NP scenarios. For this purpose, we have also calculated the full variation in the values of observables by using the 1σ to 2σ ranges of WC's of 1D scenarios after integrating the full and the different q^2 bins and are shown by the bar plots in FIG. 7. The SM values and the values in the different 1D NP scenarios of the angular observables in the full q^2 region are also given in TABLE. VI.

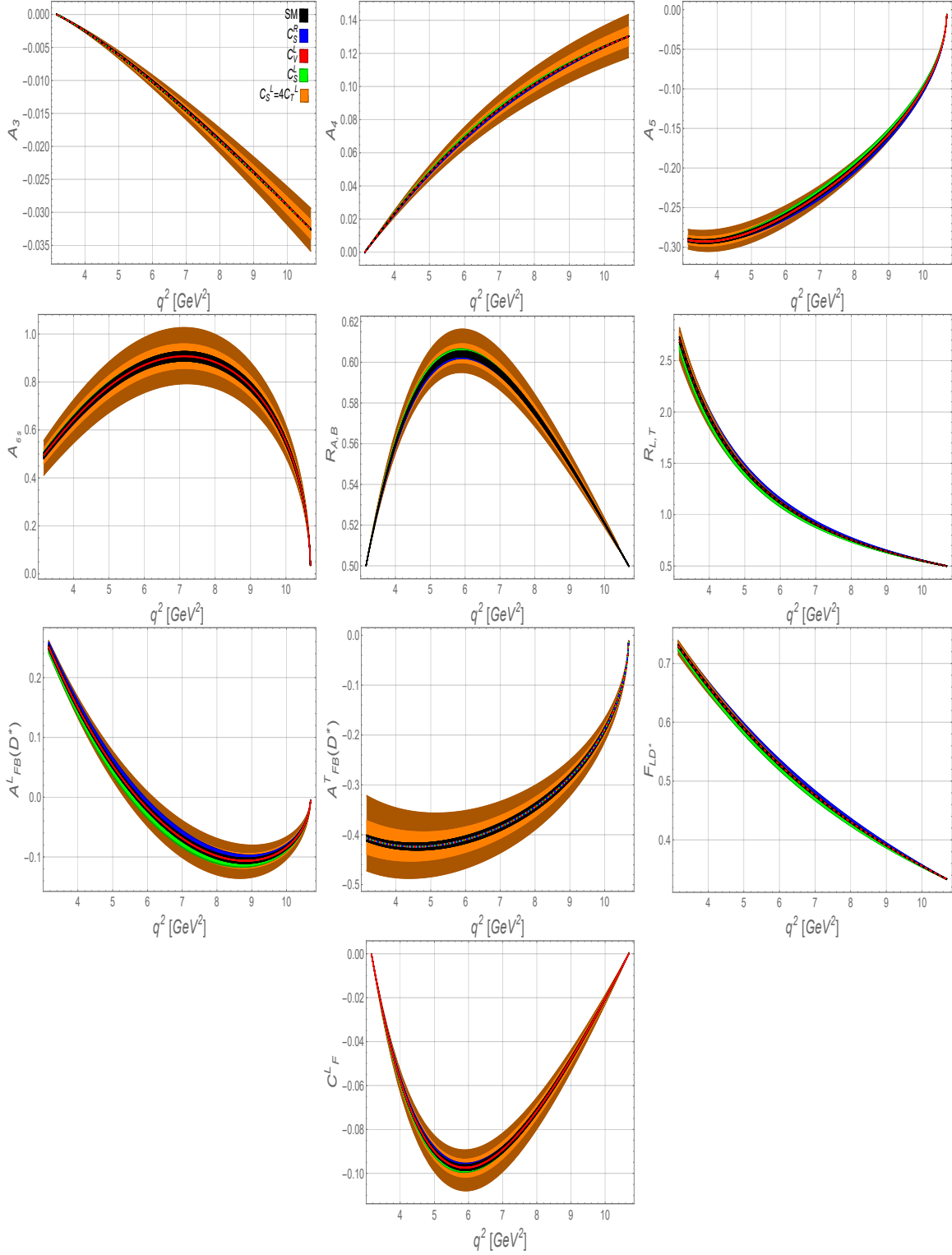


FIG. 6: A_{3-5} , A_{6s} , $R_{A,B}$, $R_{L,T}$, $A_{FB}^{L,T}(D^*)$, $F_L(D^*)$ and C_F^L for $\bar{B} \rightarrow D^* \tau \bar{\nu}$ are shown for allowed values of NP couplings for 1D scenarios as function of q^2 . The black band shows the theoretical uncertainties in the hadronic form factors while the light and dark color bands reflect the 1σ and 2σ ranges of NP scenarios.

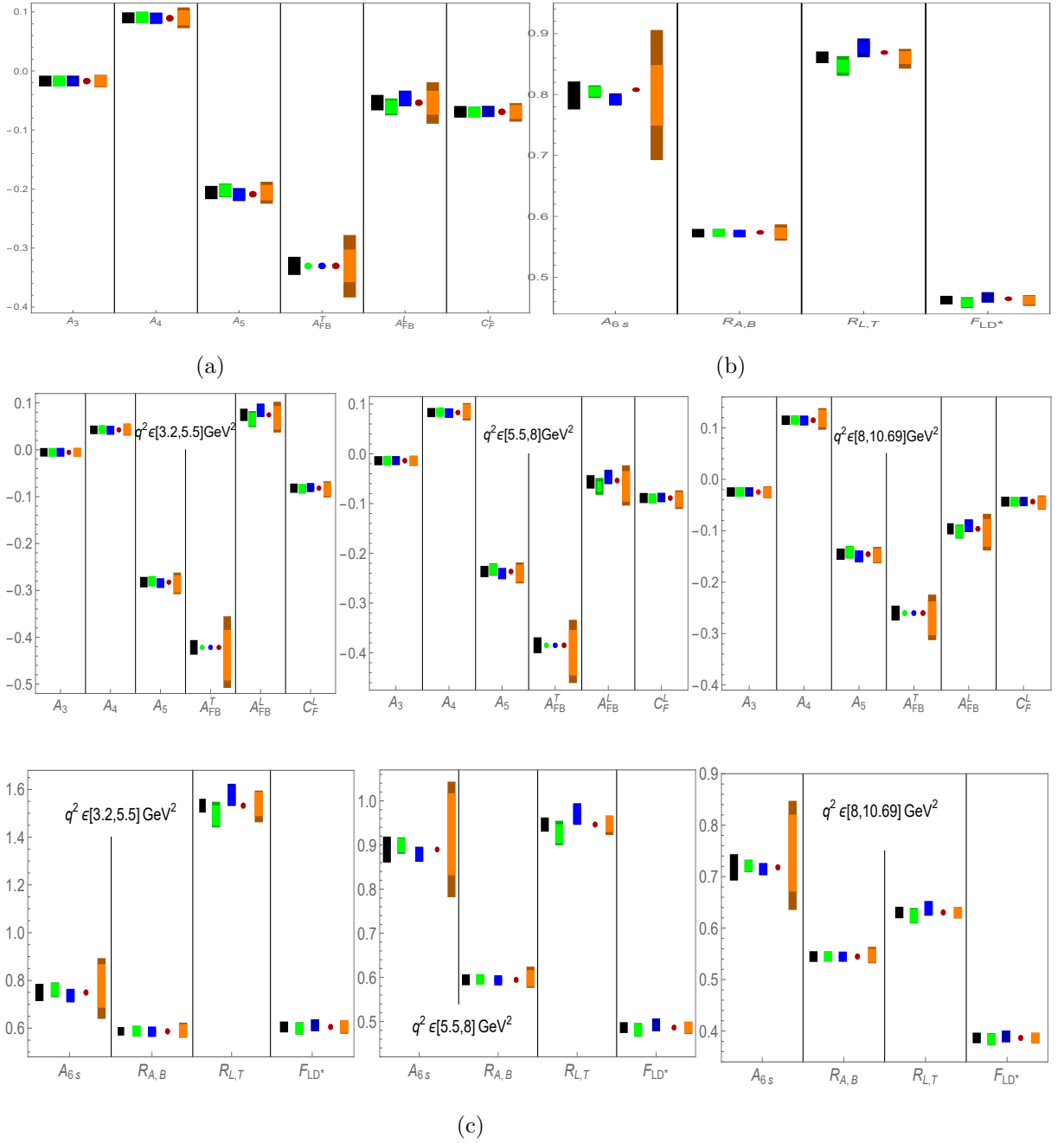


FIG. 7: The bar plots of A_{3-5} , A_{6s} , $R_{A,B}$, $R_{L,T}$, $A_{FB}^{L,T}(D^*)$, $F_L(D^*)$ and C_F^L for $\bar{B} \rightarrow D^* \tau \bar{\nu}$ are shown. The bar plots in first row show the numerical values of angular observables after integrating full q^2 while the second and third row show the numerical values in different q^2 bins. The black bar shows the SM variation of angular observables and the color bars show the variation in the numerical values in the different NP scenarios.

Observables	SM	C_S^L	C_S^R	C_V^L	$C_S^L = 4C_T$
A_3	-0.0170 ± 0.0001	-0.0172 ± 0.0001	-0.0168 ± 0.0001	-0.0170 ± 0.0001	-0.0172 ± 0.002
A_4	0.0900 ± 0.0002	0.0908 ± 0.0006	0.0892 ± 0.0006	0.0900 ± 0.0002	0.0909 ± 0.009
A_5	-0.2059 ± 0.002	-0.2020 ± 0.003	-0.2100 ± 0.002	-0.2059 ± 0.002	-0.2069 ± 0.009
A_{6s}	0.7985 ± 0.017	0.8052 ± 0.005	0.7906 ± 0.004	0.7985 ± 0.017	0.8088 ± 0.01
$R_{A,B}$	0.5725 ± 0.0009	0.5731 ± 0.0004	0.5717 ± 0.0003	0.5725 ± 0.0009	0.5732 ± 0.007
$R_{L,T}$	0.8611 ± 0.0036	0.8451 ± 0.009	0.8796 ± 0.011	0.8611 ± 0.0036	0.8621 ± 0.007
A_{FB}^T	-0.3302 ± 0.006	-0.3302 ± 0.006	-0.3302 ± 0.006	-0.3302 ± 0.006	-0.3346 ± 0.04
A_{FB}^L	-0.0536 ± 0.004	-0.0613 ± 0.005	-0.0450 ± 0.005	-0.0536 ± 0.004	-0.0562 ± 0.002
$F_L(D^*)$	0.4649 ± 0.001	0.4581 ± 0.003	0.4679 ± 0.003	0.4649 ± 0.001	0.4629 ± 0.002
C_F^L	-0.0691 ± 0.0009	-0.0697 ± 0.0007	-0.0685 ± 0.0004	-0.0691 ± 0.0009	-0.0698 ± 0.006

TABLE VI: The SM and the NP values of angular observables at 2σ allowed parametric space in the full q^2 region for different 1D scenarios.

B. Effects of 2D scenarios on observables

For the case of 2D NP scenarios, the effects on the considered angular observables are shown in Fig. 8. It is clear from the figure that the observables are not sensitive to the scenario (C_V^L, C_S^R) (red band), whereas they are influenced by the other 2D scenarios, particularly $(\text{Re}[C_S^L = 4C_T], \text{Im}[C_S^L = 4C_T])$ has large effect (cyan band) on the values of the angular observables. One can also see that the effects of NP scenarios, $(\text{Re}[C_S^L = 4C_T], \text{Im}[C_S^L = 4C_T])$ (cyan band), $(C_V^L, C_S^L = -4C_T)$ (purple band) are increased (decreased) when the q^2 value increases for A_3, A_4 ($A_5, R_{L,T}, F_L(D^*)$ and A_{FB}^T), whereas the observables $A_{6S}, R_{A,B}, A_{FB}^L$ and C_F^L are largely effected in the middle of q^2 region. Therefore, we have not only plotted the variation in the amplitude due to the 2D NP scenarios when integrated over whole q^2 region but also in different q^2 bins and shown in Fig. 9. Moreover, the scalar coupling scenario (C_S^L, C_S^R) (blue band), only increase (decrease) the values of $A_3, R_{L,T}, A_{FB}^L, F_L(D^*), C_L^F$ ($A_4, A_5, A_{6S}, R_{A,B}, A_{FB}^T$) with respect to their SM values throughout the q^2 region. On the other hand, the scenarios $(\text{Re}[C_S^L = 4C_T], \text{Im}[C_S^L = 4C_T]), (C_V^L, C_S^L = -4C_T)$, raise and lower the values of these observables values from their SM predictions throughout the q^2 region. In addition, to see the total variation in the magnitude of numerical values of different angular observables, we have also calculated their numerical values by using the 2σ parametric space of 2D scenarios and listed them in Table VII along with their SM results.

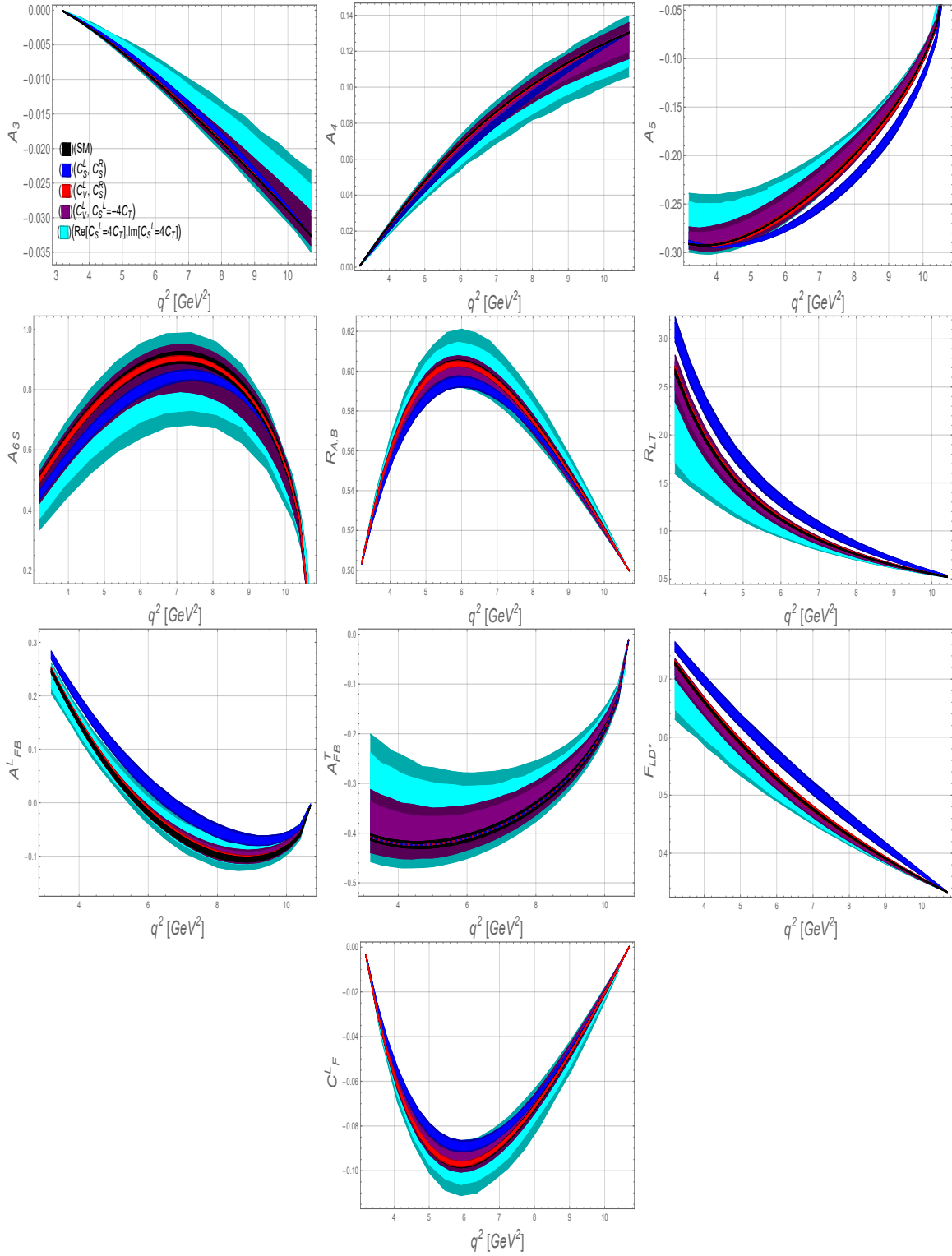


FIG. 8: The legends are same as described in FIG. 6 but for 2D scenarios.

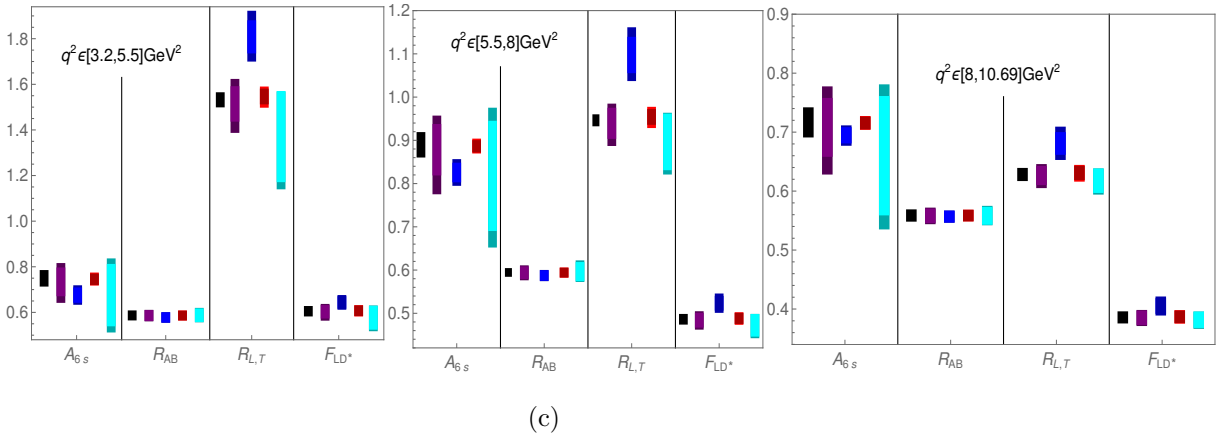
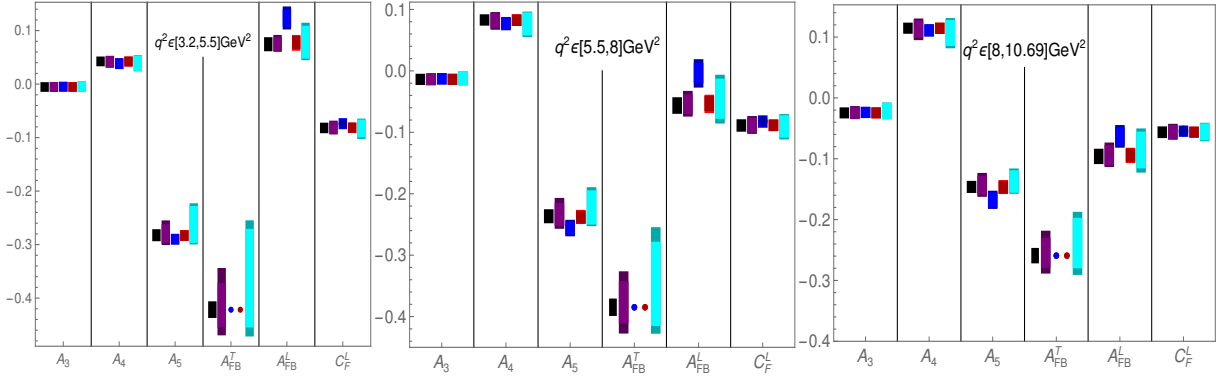
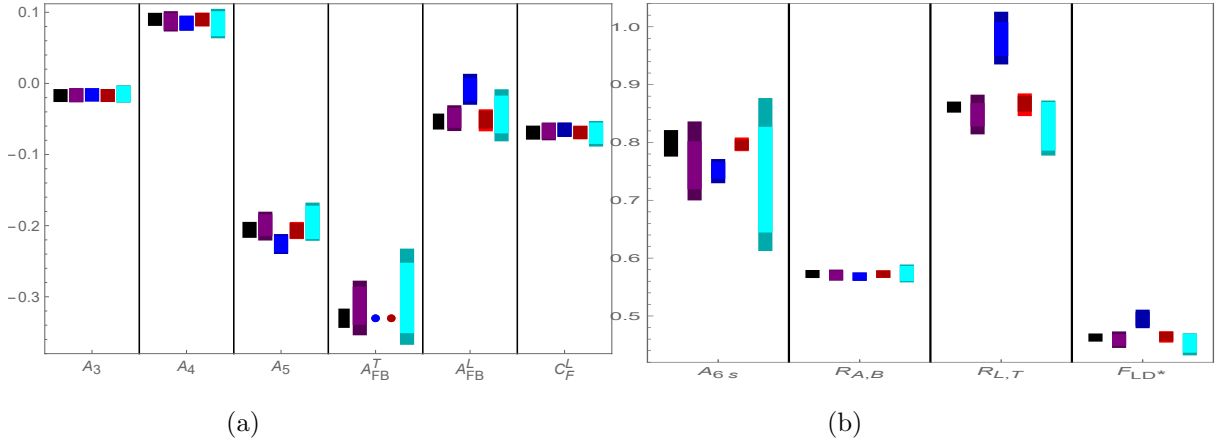


FIG. 9: The legends are same as described in FIG. 7 but for 2D scenarios.

Observables	SM	$(C_V^L, C_S^L = -4C_T)$	(C_S^L, C_S^R)	(C_V^L, C_S^L)	$(\text{Re}[C_S^L = 4C_T], \text{Im}[C_S^L = 4C_T])$
A_3	-0.0170 ± 0.0001	-0.0164 ± 0.001	-0.0160 ± 0.0003	-0.0170 ± 0.0001	-0.0140 ± 0.004
A_4	0.0900 ± 0.0002	0.0870 ± 0.005	0.0848 ± 0.002	0.898 ± 0.0007	0.0811 ± 0.009
A_5	-0.2059 ± 0.002	-0.1991 ± 0.011	-0.2257 ± 0.005	-0.2072 ± 0.003	-0.1896 ± 0.03
A_{6s}	0.7985 ± 0.017	0.7610 ± 0.058	0.7520 ± 0.013	0.7960 ± 0.006	0.7093 ± 0.011
$R_{A,B}$	0.5725 ± 0.001	0.5701 ± 0.005	0.5681 ± 0.0001	0.5723 ± 0.0006	0.5740 ± 0.008
$R_{L,T}$	0.8611 ± 0.0036	0.8453 ± 0.0026	0.9761 ± 0.04	0.8668 ± 0.012	0.8115 ± 0.03
A_{FB}^T	-0.3302 ± 0.006	-0.3121 ± 0.032	-0.3302 ± 0.006	-0.3302 ± 0.006	-0.2855 ± 0.044
A_{FB}^L	-0.0536 ± 0.004	-0.0483 ± 0.008	-0.008 ± 0.004	-0.0508 ± 0.006	-0.0398 ± 0.03
$F_L(D^*)$	0.4649 ± 0.001	0.4581 ± 0.009	0.4939 ± 0.009	0.4643 ± 0.004	0.4479 ± 0.01
C_F^L	-0.0691 ± 0.0009	-0.0670 ± 0.004	-0.0651 ± 0.0001	-0.0689 ± 0.0006	-0.0705 ± 0.009

TABLE VII: The SM and the NP values of angular observables at 2σ allowed parametric space in the full q^2 region for different 2D scenarios.

VI. SUMMARY AND CONCLUSIONS

In the current study, we have first checked the impact of recently measured data of $R(D^{(*)})$ and $R(\Lambda_c)$ [34] on different 1D and 2D NP scenarios that are considered in refs. [1–3]. In addition, we have also included the $R(J/\psi)$ and the $R(X_c)$ data in the analysis which are not considered in the previous studies and found that their influence on the best fit point and the parametric space are not significantly large. We have also validated (in light of recent data) the robustness of the sum rule of $R(\Lambda_c)$ and, similarly, found the sum rule for $R(J/\psi)$ in terms of $R(D^{(*)})$. From this sum rule, we have also predicted the value of $R(J/\psi)$ which is smaller than its experimental value. Instead, the form factors of $R(J/\psi)$ are not precisely calculated but the difference between its experimental and theoretical values is quite large, therefore, to see the agility of the sum rule of $R(J/\psi)$ and the NP, it is mandatory to confirm the $R(J/\psi)$ value from further experiments. Furthermore, we have also modified the correlation among the different observables given in ref. [1] according to the recent development in the data and also shown some more interesting correlations among observables. Finally, to discriminate the NP scenarios from each other, we have plotted the different angular observables against q^2 , by using the 1σ and 2σ parametric space of NP scenarios considered here. Further to see the influence of NP on the amplitude of the angular observables, we have also calculated their numerical values in different q^2 bins and shown them through the bar plots. We have found that angular observables are not only sensitive to NP but also very fertile to find out the precise values of possible NP couplings, consequently, helping us in discriminating various NP scenarios.

Acknowledgements

The authors would like to express their sincere gratitude to Prof. Monika Blanke *et.al.*, and Dr. Nestor Quintero for valuable feedback on our queries during the course of this study which enable us to understand their work.

VII. APPENDIX

A. Expressions of I 's

As mentioned in section V, the expressions of I_i 's can be found in [45, 74, 134]. However, I_i 's after integrating over q^2 can be expressed in terms of $C_i^{L(R)}$ as follows. These expression are given as

$$\begin{aligned}
I_1^s &= 6.02 \times 10^{-15} \left\{ |1 + C_V^L|^2 + |C_V^R|^2 - 1.63 \text{Re} \left[(1 + C_V^L) (C_V^R)^* \right] - 4.68 \text{Re} \left[(1 + C_V^L) (C_T)^* \right] \right. \\
&\quad \left. + 16.2 |C_T|^2 + 7.6 \text{Re} \left[(C_V^R) (C_T)^* \right] \right\}, \\
I_1^c &= 9.05 \times 10^{-15} \left\{ |1 + C_V^L - C_V^R|^2 + 0.08 |1 + C_S^R - C_S^L|^2 - 0.242 \text{Re} \left[(1 + C_V^L - C_V^R) (C_S^L)^* \right] \right. \\
&\quad \left. + 0.242 \text{Re} \left[(1 + C_V^L - C_V^R) (C_S^R)^* \right] - 4.07 \text{Re} \left[(1 + C_V^L - C_V^R) (C_S^R)^* \right] \right\} + 6.24 |C_T|^2 \\
I_2^c &= -5.43 \times 10^{-15} \left\{ |1 + C_V^L - C_V^R|^2 + 8.31 |C_T|^2 \right\}, \\
I_2^s &= 9.99 \times 10^{-16} \left\{ |1 + C_V^L - C_V^R|^2 - 21.7 |C_T|^2 \right\}, \\
I_3 &= 1.67 \times 10^{-15} \left\{ -|1 + C_V^L - C_V^R|^2 - 12.5 |C_T|^2 \right\}, \\
I_4 &= 2.23 \times 10^{-15} \left\{ -|1 + C_V^L - C_V^R|^2 - 12 |C_T|^2 \right\}, \\
I_5 &= 4.49 \times 10^{-15} \left\{ |1 + C_V^L - C_V^R|^2 - 5.75 |C_T|^2 + 2.04 [|C_S^L - C_S^R| C_T^*] - 1.26 \text{Re} \left[(C_V^R) (C_T)^* \right] \right\}, \\
I_6^c &= 5.44 \times 10^{-15} \left\{ |1 + C_V^L - C_V^R|^2 - 0.67 \text{Re} \left[(1 + C_V^L - C_V^R) (C_S^L)^* \right] + 0.67 \text{Re} \left[(1 + C_V^L - C_V^R) (C_S^R)^* \right] \right. \\
&\quad \left. - 3.76 \text{Re} \left[(1 + C_V^L) (C_T)^* \right] + [|C_S^L - C_S^R| C_T^*] \right\}, \\
I_6^s &= -3.85 \times 10^{-15} \left\{ |1 + C_V^L|^2 + |C_V^R|^2 - 17.5 |C_T|^2 - 2.59 \text{Re} \left[(1 + C_V^L) (C_T)^* \right] - 8.54 \text{Re} \left[(C_V^R) (C_T)^* \right] \right\}.
\end{aligned}$$

-
- [1] M. Blanke, A. Crivellin, S. de Boer, T. Kitahara, M. Moscati, U. Nierste and I. Nisandzic, Phys. Rev. D **99**, no.7, 075006 (2019) arXiv:1811.09603 [hep-ph].
- [2] M. Fedele, M. Blanke, A. Crivellin, S. Iguro, T. Kitahara, U. Nierste and R. Watanabe(2022), arXiv:2211.14172 [hep-ph].
- [3] M. Blanke, A. Crivellin, T. Kitahara, M. Moscati, U. Nierste and I. Nisandzic, Phys. Rev. D **100**, 035035 (2019) arXiv:1905.08253 [hep-ph].
- [4] R. Dutta, A. Bhol and A. K. Giri, Phys. Rev. D **88**, no.11, 114023 (2013) arXiv:1307.6653 [hep-ph].
- [5] R. Dutta and A. Bhol, Phys. Rev. D **96**, no.7, 076001 (2017) arXiv:1701.08598 [hep-ph].
- [6] R. Dutta, arXiv:1710.00351 [hep-ph].

- [7] R. Dutta and N. Rajeev, Phys. Rev. D **97**, no.9, 095045 (2018) arXiv:1803.03038 [hep-ph].
- [8] A. Azatov, D. Barducci, D. Ghosh, D. Marzocca and L. Ubaldi, JHEP **1810** 092, (2018) arXiv:1807.10745 [hep-ph].
- [9] J. Heeck and D. Teresi, JHEP **1812** 103, (2018) arXiv:1808.07492 [hep-ph].
- [10] X. Qiang Li, Y. D. Yang and X. Zhang, JHEP **1608**, 054 (2016) arXiv:1605.09308 [hep-ph].
- [11] R. Aaij *et al.* [LHCb Collaboration], Phys. Rev. Lett. **113**, 151601 (2014) arXiv:1406.6482 [hep-ex].
- [12] Y. Sakaki, M. Tanaka, A. Tayduganov and R. Watanabe, Phys. Rev. D **88**, no. 9, 094012 (2013) arXiv:1309.0301 [hep-ph].
- [13] I. Caprini, L. Lellouch and M. Neubert, Nucl. Phys. B **530**, 153 (1998) [hep-ph/9712417].
- [14] J. A. Bailey *et al.* [Fermilab Lattice and MILC Collaborations], Phys. Rev. D **89**, no. 11, 114504 (2014) arXiv:1403.0635 [hep-lat].
- [15] Z. Ligeti, M. Papucci and D. J. Robinson, JHEP **1701** 083, (2017) arXiv:1610.02045 [hep-ph].
- [16] A. Abdesselam *et al.* [Belle Collaboration], arXiv:1903.03102 [hep-ex].
- [17] A. Abdesselam *et al.* arXiv:1904.08794 [hep-ex].
- [18] R. Aaij *et al.* [LHCb Collaboration], Phys. Rev. Lett. **120**, 121801 (2018) arXiv:1711.05623 [hep-ex].
- [19] C. W. Murphay and A. Soni, (2018) arXiv:1808.05392 [hep-ph].
- [20] S. Kamali, A. Rashed, and A. Datta, Phys. Rev. D. **97**, no. 9, 095034 (2018), arXiv:1801.08259 [hep-ph].
- [21] Y. Grossman and Z. Ligeti, Phys. Lett. **B332** 373–380 (1994) , arXiv:hep-ph/9403376 [hep-ph].
- [22] P. Colangelo and F. De Fazio, Phys. Rev. D. **95** no. 1, 011701 (2017) arXiv:1611.07387 [hep-ph].
- [23] R. Aaij *et al.* [LHCb Collaboration], Phys. Rev. Lett. **128**,no. 19, 191803 (2022)
- [24] W. Detmold, C. Lehner, and S. Meinel, Phys. Rev. D **92**, 034503 (2015), arXiv:1503.01421 [hep-lat].
- [25] J. P. Lees *et al.* [BaBar Collaboration], Phys. Rev. Lett. **109**, 101802 (2012) arXiv:1205.5442 [hep-ex].
- [26] J. P. Lees *et al.* [BaBar Collaboration], Phys. Rev. D **88**,no. 7, 072012 (2013) arXiv:1303.0571 [hep-ex].
- [27] M. Huschle *et al.* [Belle Collaboration], Phys. Rev. D **92**, no. 7, 072014 (2015) arXiv:1507.03233 [hep-ex].
- [28] Y. Sato *et al.* [Belle Collaboration], Phys. Rev. D **94**, no. 7, 072007 (2016) arXiv:1607.07923 [hep-ex].
- [29] A. Abdesselam *et al.*, arXiv:1608.06391 [hep-ex].
- [30] G. Caria *et al.*, [Belle collaboration] Phys. Rev. Lett. **124** (2020) 161803, arXiv:1910.05864.
- [31] G. Caria *et al.* [Belle Collaboration], Phys. Rev. Lett. **124**, no. 16, 161803 (2020) arXiv:1910.05864 [hep-ex].
- [32] R. Aaij *et al.* [LHCb Collaboration], Phys. Rev. Lett. **115**, no. 11, 111803 (2015) arXiv:1506.08614 [hep-ex].
- [33] R. Aaij *et al.* [LHCb Collaboration], arXiv:1708.08856 [hep-ex].
- [34] Preliminary average of $R(D)$ and $R(D^*)$ for Summer2023, <https://hflav-eos.web.cern.ch/hflav-eos/semi/summer23/html/RDsDsstar/RDRDs.html>.
- [35] S. Fajfer, J. F. Kamenik and I. Nisandzic, Phys. Rev. D **85**, 094025 (2012) arXiv:1203.2654 [hep-ph].
- [36] J. F. Kamenik and F. Mescia, Phys. Rev. D **78**, 014003 (2008) arXiv:0802.3790 [hep-ph].
- [37] Y. Amhis *et al.* [Heavy Flavor Averaging Collaboration], Eur. Phys. J. C **77**,no.12, 895 (2017) arXiv:1612.07233 [hep-ph].
- [38] J. A. Bailey *et al.*, Phys. Rev. Lett. **109**, 071802 (2012) arXiv:1206.4992 [hep-ph].
- [39] J. A. Bailey *et al.* [MILC Collaboration] Phys. Rev. D. **92**, no.3, 034506 (2015) arXiv:1503.07237 [hep-ph].
- [40] S. Aoki *et al.* Eur. Phys. J. C **77**, no. 2, 112 (2017) arXiv:1607.00299 [hep-lat].
- [41] S. Hirose *et al.* [BELLE], Phys. Rev. Lett. **118**, 211801 (2017) arXiv:1612.00529 [hep-ex].

- [42] S. Hirose *et al.*[BELLE], Phys. Rev. D. **97**, 012004 (2018) arXiv:1709.00529 [hep-ex]
- [43] M. Tanaka and R. Watanabe, Phys. Rev. D **87**, no. 3, 034028 (2013) arXiv:1212.1878 [hep-ph].
- [44] P. Asadi, M. R. Buckley and D. Shih, arXiv:1810.06597 [hep-ph].
- [45] A. K. Alok, D. Kumar, S. Kumbhakar, and S. U. Sankar, Phys. Rev. D. **95**, 115038 (2017) arXiv:1606.03164 [hep-ph].
- [46] M. Tanaka and R. Watanabe, Phys. Rev. D **82**, 034027 (2010) arXiv:1005.4306 [hep-ph].
- [47] LHCb-PAPER-2017-035.
- [48] Presentation by M. Fontana, on behalf of LHCb Collaboration, [talk slide].
- [49] R. Watanabe, Phys. Rev. Lett. **B 776**, no. 5 (2018) arXiv:1709.08644 [hep-ph].
- [50] B. Chauhan and B. Kindra, (2017) arXiv:1709.09989 [hep-ph].
- [51] T. D. Cohen, H. Lamm, and R. F. Lebed, JHEP **09**, 168 (2018) arXiv:1807.02730 [hep-ph].
- [52] C. T. Tran, M. A. Ivanov, J. G. Korner, and P. Santorelli, Phys. Rev. D. **97**, 054014 (2018) arXiv:1801.06927 [hep-ph].
- [53] A. Issadykov and M. A. Ivanov, Phys. Part. Nucl. Lett. **20**, no.3, 355-359 (2023) [arXiv:2307.05013 [hep-ph]].
- [54] K. Azizi, Y. Sarac and H. Sundu, Phys. Rev. D **99**, no.11, 113004 (2019) doi:10.1103/PhysRevD.99.113004 [arXiv:1904.08267 [hep-ph]].
- [55] K. Adamczyk, (2018) talk at 10th International Workshop on the CKM unitarity Triangle, Heidelberg, 17-21 Sep. 2018.
- [56] A. Celis, M. Jung, X. Q. Li and A. Pich, Phys. Lett. B **771**, 168 (2017) arXiv:1612.07757 [hep-ph].
- [57] P. Asadi, M. R. Buckley and D. Shih, JHEP **1809**, 010 (2018) [arXiv:1804.04135 [hep-ph]].
- [58] S. Iguro, T. Kitahara, Y. Omura, R. Watanabe and K. Yamamoto, JHEP **1902**, 194 (2019) arXiv:1811.08899 [hep-ph].
- [59] R. Alonso, B. Grinstein and J. Martin Camalich, Phys. Rev. Lett. **118**, no. 8, 081802 (2017) arXiv:1611.06676 [hep-ph].
- [60] A. G. Akeroyd and C. H. Chen, Phys. Rev. D **96**, no. 7, 075011 (2017) arXiv:1708.04072 [hep-ph].
- [61] S. S. Gershtein, V. V. Kiselev, A. K. Likhoded, and A. V. Tkabladze, Phys. Usp. **38**, 1 (1995),
- [62] I. I. Y. Bigi, Phys. Lett. B **371**, 105 (1996), arXiv:hep-ph/9510325 [hep-ph].
- [63] M. Beneke and G. Buchalla, Phys. Rev. D **53**, 4991 (1996), arXiv:hep-ph/9601249 [hep-ph].
- [64] C.-H. Chang, S.-L. Chen, T.-F. Feng, and X.-Q. Li, Phys. Rev. D **64**, 014003 (2001), arXiv:hep-ph/0007162 [hep-ph].
- [65] V. V. Kiselev, A. E. Kovalsky, and A. K. Likhoded, Nucl. Phys. B **585**, 353 (2000), arXiv:hep-ph/0002127 [hep-ph].
- [66] S. Iguro, T. Kitahara and R. Watanabe, [arXiv:2210.10751 [hep-ph]].
- [67] HPQCD Collaboration, Phys. Rev. D **102** (2020) 094518 [arXiv:2007.06957]
- [68] LATTICE-HPQCD Collaboration, Phys. Rev. Lett. **125** (2020) 222003 [arXiv:2007.06956].
- [69] S. Kamali, Int. J. Mod. Phys. A **34**, no. 06, 1950036 (2019) arXiv:1811.07393 [hep-ph].
- [70]] LHCb Collaboration, Phys. Rev. Lett. **128** (2022) 191803 [arXiv:2201.03497].
- [71] R. X. Shi, L. S. Geng, B. Grinstein, S. Jager and J. Martin Camalich, JHEP **1912**, 065 (2019) arXiv:1905.08498 [hep-ph].
- [72] T. Bhattacharya, V. Cirigliano, S. D. Cohen, A. Filipuzzi, M. Gonzalez-Alonso, et al. Phys. Rev. D **85**,

- 054512,(2012) arXiv:1110.6448 [hep-ph].
- [73] FlaviaNet Working Group on Kaon Decays Collaboration, M. Antonelli et al., Italy, 7-10 April 2008, 2008. arXiv:0801.1817 [hep-ph].
- [74] B. Damir, M. Fedele, I. Nisandzic and A. Tayduganov arXiv:1907.02257 [hep-ph].
- [75] L. Zhang, X. W. Kang, X. H. Guo, L. Y. Dai, T. Luo and C. Wang, *JHEP* **02**, 179 (2021) doi:10.1007/JHEP02(2021)179 [arXiv:2012.04417 [hep-ph]].
- [76] R. N. Faustov, V. O. Galkin and X. W. Kang, *Phys. Rev. D* **106**, no.1, 013004 (2022) doi:10.1103/PhysRevD.106.013004 [arXiv:2206.10277 [hep-ph]].
- [77] J. Cardozo, J. H. Munoz, N. Quintero, E. Rojas, *J. Phys. G: Nucl. Part. Phys.* **48**, 035001 (2021). arXiv:2006.07751 [hep-ph]
- [78] J. D. Gomez, N. Quintero and E. Rojas, *Phys. Rev. D* **100** (2019) no.9, 093003 arXiv:1907.08357 [hep-ph].
- [79] B. Y. Cui, Y. K. Huang, Y. M. Wang and X. C. Zhao, [arXiv:2301.12391 [hep-ph]].
- [80] Belle II Collaboration: presented at Lepton Photon 2023 [Lepton Photon 2023]
- [81] LHCb Collaboration: accepted by PRL [arXiv:2302.02886]
- [82] LHCb Collaboration: accepted by PRD [arXiv:2305.01463]
- [83] R. Aaij et al. (LHCb), *Phys. Rev. Lett.* **120**, 121801 (2018), arXiv:1711.05623 [hep-ex].
- [84] M. Jung and D. M. Straub, *JHEP* **01** (2019) 009, arXiv:1801.01112 [hep-ph].
- [85] C. Murgui, A. Peñuelas, M. Jung and A. Pich, *JHEP* **09**, 103 (2019) doi:10.1007/JHEP09(2019)103 [arXiv:1904.09311 [hep-ph]].
- [86] M. Gonzalez-Alonso, J. Martin Camalich and K. Mimouni, *Phys. Lett. B* **772** (2017), 777-785 [arXiv:1706.00410 [hep-ph]].
- [87] A. Datta, S. Kamali, S. Meinel, and A. Rashed, *JHEP* **08** (2017) 131 [arXiv:1702.02243 [hep-ph]].
- [88] R. Alonso, B. Grinstein, and J. Martin Camalich, *JHEP* **10**, 184 (2015) arXiv:1505.05164 [hep-ph]
- [89] L. Calibbi, A. Crivellin, and T. Ota, *Phys. Rev. Lett.* **115**, 181801 (2015), arXiv:1506.02661 [hep-ph].
- [90] S. Fajfer and N. Kořnik, *Phys. Lett. B* **755**, 270 (2016), arXiv:1511.06024 [hep-ph].
- [91] R. Barbieri, G. Isidori, A. Pattori, and F. Senia, *Eur. Phys. J. C* **76**, 67 (2016), arXiv:1512.01560 [hep-ph].
- [92] R. Barbieri, C. W. Murphy, and F. Senia, *Eur. Phys. J. C* **77**, 8 (2017), arXiv:1611.04930 [hep-ph]
- [93] G. Hiller, D. Loose, and K. Schonwald, *JHEP* **12**, 027 (2016), arXiv:1609.08895 [hep-ph].
- [94] B. Bhattacharya, A. Datta, J.-P. Guévin, D. London, and R. Watanabe, *JHEP* **01**, 015 (2017), arXiv:1609.09078 [hep-ph].
- [95] D. Buttazzo, A. Greljo, G. Isidori, and D. Marzocca, *JHEP* **11**, 044 (2017), arXiv:1706.07808 [hep-ph]
- [96] J. Kumar, D. London, and R. Watanabe, (2018), arXiv:1806.07403 [hep-ph]
- [97] N. Assad, B. Fornal, and B. Grinstein, *Phys. Lett. B* **777**, 324 (2018), arXiv:1708.06350 [hep-ph].
- [98] L. Di Luzio, A. Greljo, and M. Nardecchia, *Phys. Rev. D* **96**, 115011 (2017), arXiv:1708.08450 [hep-ph].
- [99] L. Calibbi, A. Crivellin, and T. Li, (2017), arXiv:1709.00692 [hep-ph].
- [100] M. Bordone, C. Cornella, J. Fuentes-Martin, and G. Isidori, *Phys. Lett. B* **779**, 317 (2018), arXiv:1712.01368 [hep-ph]
- [101] R. Barbieri and A. Tesi, *Eur. Phys. J. C* **78**, 193 (2018), arXiv:1712.06844 [hep-ph]
- [102] M. Blanke and A. Crivellin, *Phys. Rev. Lett.* **121**, 011801 (2018), arXiv:1801.07256 [hep-ph].
- [103] A. Greljo and B. A. Stefanek, *Phys. Lett. B* **782**, 131 (2018), arXiv:1802.04274 [hep-ph].

- [104] M. Bordone, C. Cornella, J. Fuentes-Martín, and G. Isidori, (2018), arXiv:1805.09328 [hep-ph]
- [105] S. Matsuzaki, K. Nishiwaki, and K. Yamamoto, (2018), arXiv:1806.02312 [hep-ph].
- [106] A. Crivellin, C. Greub, F. Saturnino, and D. Muller, (2018), arXiv:1807.02068 [hep-ph]
- [107] L. Di Luzio, J. Fuentes-Martin, A. Greljo, M. Nardecchia, and S. Renner, (2018), arXiv:1808.00942 [hep-ph]
- [108] A. Biswas, D. Kumar Ghosh, N. Ghosh, A. Shaw, and A. K. Swain, (2018), arXiv:1808.04169 [hep-ph]
- [109] N. G. Deshpande and A. Menon, JHEP 01, 025 (2013), arXiv:1208.4134 [hep-ph]. [hep-ph].
- [110] M. Bauer and M. Neubert, Phys. Rev. Lett. 116, 141802 (2016), arXiv:1511.01900 [hep-ph]
- [111] Y. Cai, J. Gargalionis, M. A. Schmidt, and R. R. Volkas, JHEP 10, 047 (2017), arXiv:1704.05849 [hep-ph]
- [112] A. Crivellin, D. Muller, and T. Ota, JHEP 09, 040 (2017), arXiv:1703.09226 [hep-ph]
- [113] W. Altmannshofer, P. Bhupal Dev, and A. Soni, Phys. Rev. D96, 095010 (2017), arXiv:1704.06659 [hep-ph].
- [114] D. Marzocca, JHEP 07, 121 (2018), arXiv:1803.10972 [hep-ph]
- [115] X.-G. He and G. Valencia, Phys. Rev. D87, 014014 (2013), arXiv:1211.0348 [hep-ph].
- [116] A. Greljo, G. Isidori, and D. Marzocca, JHEP 07, 142 (2015), arXiv:1506.01705 [hep-ph].
- [117] S. M. Boucenna, A. Celis, J. Fuentes-Martin, A. Vicente, and J. Virto, Phys. Lett. B760, 214 (2016), arXiv:1604.03088 [hep-ph]
- [118] X.-G. He and G. Valencia, Phys. Lett. B779, 52 (2018), arXiv:1711.09525 [hep-ph]
- [119] J. Kalinowski, Phys. Lett. B245, 201 (1990).
- [120] W.-S. Hou, Phys. Rev. D48, 2342 (1993).
- [121] N. Kosnik, Phys. Rev. D86, 055004 (2012), arXiv:1206.2970 [hep-ph]
- [122] A. Biswas, A. Shaw, and A. K. Swain, (2018), arXiv:1811.08887 [hep-ph].
- [123] A. Crivellin, C. Greub, and A. Kokulu, Phys. Rev. D86, 054014 (2012), arXiv:1206.2634 [hep-ph].
- [124] A. Crivellin, A. Kokulu, and C. Greub, Phys. Rev. D87, 094031 (2013), arXiv:1303.5877 [hep-ph].
- [125] A. Celis, M. Jung, X.-Q. Li, and A. Pich, JHEP 01, 054 (2013), arXiv:1210.8443 [hep-ph].
- [126] P. Ko, Y. Omura, and C. Yu, JHEP 03, 151 (2013), arXiv:1212.4607 [hep-ph].
- [127] A. Crivellin, J. Heeck, and P. Stoffer, Phys. Rev. Lett. 116, 081801 (2016), arXiv:1507.07567 [hep-ph].
- [128] L. Dhargyal, Phys. Rev. D93, 115009 (2016), arXiv:1605.02794 [hep-ph].
- [129] C.-H. Chen and T. Nomura, Eur. Phys. J. C77, 631 (2017), arXiv:1703.03646 [hep-ph].
- [130] S. Iguro and K. Tobe, Nucl. Phys. B925, 560 (2017), arXiv:1708.06176 [hep-ph]
- [131] R. Martinez, C. F. Sierra, and G. Valencia, (2018), arXiv:1805.04098 [hep-ph].
- [132] A. Biswas, D. K. Ghosh, A. Shaw, and S. K. Patra, (2018), arXiv:1801.03375 [hep-ph].
- [133] D. Leljak, B. Melic, and M. Patra, JHEP 05 (2019) 094 arXiv:1901.08368[hep-ph].
- [134] R. Mandal, C. Murgui, A. Penuelas and A. Pich, JHEP 08, 022 (2020) arXiv:2004.06726 [hep-ph].
- [135] D. Becirevic, I. Dorsner, S. Fajfer, N. Kosnik, D. A. Faroughy, and O. Sumensari, Phys. Rev. D98, 055003 (2018), arXiv:1806.05689 [hep-ph].
- [136] R. Alonso, E. E. Jenkins, A. V. Manohar, and M. Trott, JHEP 04, 159 (2014), arXiv:1312.2014 [hep-ph].